



HAL
open science

Metamorphic brines and no surficial fluids trapped in the detachment footwall of a Metamorphic Core Complex (Nevado-Filábride units, Betics, Spain)

Vanessa Dyja-Person, Alexandre Tarantola, Antonin Richard, Christian Hibsich, Luc Siebenaller, Marie-Christine Boiron, Michel Cathelineau, Philippe Boulvais

► To cite this version:

Vanessa Dyja-Person, Alexandre Tarantola, Antonin Richard, Christian Hibsich, Luc Siebenaller, et al.. Metamorphic brines and no surficial fluids trapped in the detachment footwall of a Metamorphic Core Complex (Nevado-Filábride units, Betics, Spain). *Tectonophysics*, 2018, 727, pp.56-72. 10.1016/j.tecto.2018.02.001 . insu-01713218

HAL Id: insu-01713218

<https://insu.hal.science/insu-01713218v1>

Submitted on 3 Nov 2024

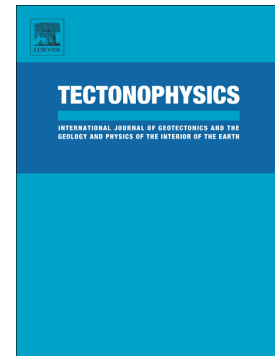
HAL is a multi-disciplinary open access archive for the deposit and dissemination of scientific research documents, whether they are published or not. The documents may come from teaching and research institutions in France or abroad, or from public or private research centers.

L'archive ouverte pluridisciplinaire **HAL**, est destinée au dépôt et à la diffusion de documents scientifiques de niveau recherche, publiés ou non, émanant des établissements d'enseignement et de recherche français ou étrangers, des laboratoires publics ou privés.

Accepted Manuscript

Metamorphic brines and no surficial fluids trapped in the detachment footwall of a Metamorphic Core Complex (Nevado-Filábride units, Betics, Spain)

Vanessa Dyja-Person, Alexandre Tarantola, Antonin Richard, Christian Hibsich, Luc Siebenaller, Marie-Christine Boiron, Michel Cathelineau, Philippe Boulvais



PII: S0040-1951(18)30062-3
DOI: <https://doi.org/10.1016/j.tecto.2018.02.001>
Reference: TECTO 127773
To appear in: *Tectonophysics*
Received date: 24 February 2017
Revised date: 29 January 2018
Accepted date: 1 February 2018

Please cite this article as: Vanessa Dyja-Person, Alexandre Tarantola, Antonin Richard, Christian Hibsich, Luc Siebenaller, Marie-Christine Boiron, Michel Cathelineau, Philippe Boulvais, Metamorphic brines and no surficial fluids trapped in the detachment footwall of a Metamorphic Core Complex (Nevado-Filábride units, Betics, Spain). The address for the corresponding author was captured as affiliation for all authors. Please check if appropriate. Tecto(2017), <https://doi.org/10.1016/j.tecto.2018.02.001>

This is a PDF file of an unedited manuscript that has been accepted for publication. As a service to our customers we are providing this early version of the manuscript. The manuscript will undergo copyediting, typesetting, and review of the resulting proof before it is published in its final form. Please note that during the production process errors may be discovered which could affect the content, and all legal disclaimers that apply to the journal pertain.

**Metamorphic brines and no surficial fluids trapped in the detachment footwall of a
Metamorphic Core Complex (Nevado-Filábride units, Betics, Spain)**

Vanessa Dyja-Person ¹, Alexandre Tarantola ¹, Antonin Richard ¹, Christian Hibsich ¹, Luc Siebenaller ², Marie-Christine Boiron ¹, Michel Cathelineau ¹ and Philippe Boulvais ³

¹GeoRessources, Université de Lorraine, CNRS, CREGU, UMR 7359, Vandœuvre-lès-Nancy, F-54506, France

²Geosciences Environnement Toulouse (UPS GET), IRD, CNRS, Université de Toulouse, 14, av. Edouard Belin, 31400 Toulouse, France

³Université de Rennes 1, Géosciences Rennes - UMR CNRS 6118, OSUR, 35042 Rennes Cedex, France

Abstract

The ductile-brittle transition zone in extensional regimes can play the role of a hydrogeological barrier. Quartz veins developed within an orthogneiss body located in the detachment footwall of a Metamorphic Core Complex (MCC) in the Nevado-Filábride units (Betics, Spain). The detachment footwall is composed mainly of gneisses, schists and metacarbonates from the Bédar-Macael sub-unit. Schist and metacarbonate bodies show evidence of ductile deformation at the time the gneiss was already undergoing brittle deformation and vein opening during exhumation. The vein system provides the opportunity to investigate the origin, composition and *PVTX* conditions of the fluids that circulated in the detachment footwall while the footwall units were crossing the ductile-brittle transition.

The analysis of fluid inclusions reveals the presence of a single type of fluid: 30 - 40 mass% NaCl>KCl>CaCl₂>MgCl₂ brines, with trace amounts of CO₂ and N₂ and tens to thousands of ppm of metals such as Fe, Sr, Li, Zn, Ba, Pb and Cu. δD_{fluid} values between -39.8 and -16.7 ‰ and $\delta^{18}O_{\text{fluid}}$ values between 4.4 and 11.7 ± 0.5 ‰ show that the brines have undergone protracted interaction with the host orthogneissic body. Coupled salinity and Cl/Br ratios (200 to 4400) indicate that the brines originate from dissolution of Triassic metaevaporites by metamorphic fluids variably enriched in Br by interaction with graphitic schists.

This study highlights the absence of any record of surficial fluids within the veins, despite the brittle deformation conditions prevailing in this orthogneiss body. The fact that fluids from the detachment footwall were isolated from surficial fluid reservoirs may result from the presence of overlying schists and metacarbonates that continued to be affected by ductile deformation during vein formation in the gneiss, preventing downward circulation of surface-derived fluids.

Keywords

Metamorphic core complex ; Ductile-brittle transition ; Brines ; Fluid inclusions ; Betics

1. Introduction

Faults and shear zones are important conduits for fluid circulation within the Earth's crust (e.g. Kerrich, 1986; Reynolds and Lister, 1987; McCaig, 1988). Reciprocally the presence of fluids plays a major role on the deformation regime and on the localisation of deformation (e.g. Tobisch et al., 1991; Hirth and Tullis, 1992; Famin et al., 2004; Loreto et al., 2007; Mezri et al., 2015; Stünitz et al., 2017; Scheffer et al., 2017). The position of the ductile-brittle transition (DBT) evolves during exhumation of Metamorphic Core Complexes (MCC) and is controlled by the geothermal gradient and the lithological composition of the crust (Brace and Kohlstedt, 1980; Kohlstedt et al., 1995). Low-angle mylonitic-cataclastic detachments separating faulted tilted blocks from foliated metamorphic rocks are interpreted to record the transition from a brittle to a ductile behaviour respectively (Wernicke, 1981; Miller et al., 1983; Davies et al., 1986; Lister et al., 1986; Brun et al., 1994). The DBT separates a mid-crustal low-permeability reservoir of metamorphic, magmatic and mantle fluids under lithostatic pressure from an upper-crustal high-permeability fractured reservoir of predominantly surface-derived fluids under hydrostatic conditions. The downward percolation of surficial fluids below the DBT is limited by a dramatic decrease of permeability (Ingebritsen and Manning, 2002; Manning and Ingebritsen, 1999). However, the percolation of surface-derived fluids within the ductile crust along low-angle normal faults has been demonstrated, mainly through geochemical isotopic and/or fluid inclusion evidence (e.g. Kerrich et al., 1984; Wickham et al., 1993; Morrison, 1994; Upton et al., 1995; Ingebritsen and Manning, 1999; Famin et al., 2004, 2005; Siebenaller et al., 2013; Menzies et al., 2014, 2016; Dyja et al., 2016).

In this context, most fluid inclusion studies have dealt with fluids within the detachment or its hanging-wall (Famin and Nakashima, 2004; Vapnik and Avigad, 2004). There are few fluid inclusion studies focusing on the footwalls of detachments (Siebenaller et al., 2013, 2016). The main reason is that, below the detachment and the DBT, quartz veins are likely deformed and recrystallized by ductile shearing. Fluid inclusions are most commonly studied in quartz veins

(Drury and Urai, 1990), but ductile processes frequently cause the displacement of primary fluid inclusions towards grain boundaries and may alter the original fluid properties (Kerrick, 1976; Wilkins and Barkas, 1978; Johnson and Hollister, 1995).

In the internal zones of the Betic Cordillera (Spain), a major imbricated detachment system, the Mecina-Filabres detachment, separates metamorphic units referred to as the Nevado-Filábride nappes in the footwall from the Alpujarrides nappes in the hanging-wall (Martínez-Martínez et al., 2002) (Fig. 1). The footwall units crop out mainly within E-W-trending dome-shaped structures, the most important being composed of three ranges: Sierra Nevada, Sierra de los Filabres and Sierra Bédar. Within the Bédar-Macael sub-unit (Sierra Bédar), a km-scale orthogneissic body is accompanied by graphitic schists, serpentinites, metabasites and metacarbonates just below the Mecina-Filabres detachment. This orthogneiss shows quartz veins parallel and discordant to the foliation. In order to investigate the origin and *PVTX* conditions of fluids that circulated in the detachment footwall while the footwall units were crossing the ductile-brittle transition, detailed microstructural, mineralogical and geochemical characteristics of the quartz veins and their enclosed fluid inclusions were carried out.

2. Geological context and sampling

The Betic Cordillera in Southern Spain results from the convergence between Africa and Eurasia since Late Cretaceous times (Dewey et al., 1989; Vera 2001; Martínez-Martínez et al. 2002; Jolivet et al., 2003; Faccena et al., 2003), and forms an Alpine tectonic wedge that reaches a thickness of about 60 km (Platt, 2007; Jolivet et al., 2008). The internal Alboran domain is divided into three main tectono-metamorphic units, from bottom to top (Fig. 1a): the Nevado-Filábride, the Alpujarride and the Malaguide units (Egeler and Simon, 1969). These units were exhumed in relation with extensional tectonic unroofing after an isostatic rebound which is supposed to have resulted from partial or complete delamination of the lithospheric mantle (Platt, 2007). Exhumation

started during early Miocene times according to some authors (Martínez-Martínez and Azañón, 2002; Gomez-Pugnaire et al., 2004; Platt, 2007) or during late Oligocene times for others (Augier et al., 2005a). Major tectonic contacts juxtapose structural units showing different degrees of metamorphism. The unmetamorphosed Malaguide unit lies on top of the Alpujarride HP-LT metamorphic rocks along the Malaguide-Alpujarride contact. The Alpujarride HP-LT unit lies on top of the higher grade Nevado-Filábride unit along the Mecina-Filabres detachment system (Martínez-Martínez et al., 2002). The Nevado-Filábride unit was exhumed during the middle Miocene after the Alpujarride unit (Crespo-Blanc et al., 1994; Augier et al., 2005c; Platt et al., 2006). This unit can be divided into different sub-units separated by shear zones either related to older thrust contacts or more recent detachments. Three main sub-units can be recognized from bottom to top, the Ragua, Montenegro-Calar-Alto and Bédar-Macael nappes (Fig. 1a). Dating of syntectonic phengites related to top to the west shearing indicates that the Bédar-Macael sub-unit passed through the DBT during the Langhian (14 Ma) (Augier et al., 2005a). At the regional scale, ductile shearing related to exhumation stages affected the footwall of the Mecina-Filabres detachment with transport direction top towards WSW to SW (Crespo-Blanc et al., 1994; Martínez-Martínez and Azañón, 2002; Augier et al., 2005b; Platt, 2007) (Fig. 1b). Detachments are currently folded since they are implicated in E-W elongated structures such as the Sierra de los Filabres – Sierra Nevada – Sierra Bédar first-order dome (150 km long, 40 km large) (Fig. 1a) (Zeck et al., 1999; Augier et al., 2005a). The initiation of the doming is supposed to have started during the middle of the Burdigalian, as revealed by the divergence of ductile transport directions under greenschist facies conditions within the footwall on both sides of the dome (Fig. 1b) (Augier et al., 2005a,c). Thereafter, the accentuation of the dome was possibly associated with an uplift related to gravity-driven N-S-trending brittle extension until the middle of Tortonian times, but took place mainly due to more recent shortening events especially active during Messinian times with horizontal principal strains ranging from NW-SE to N-S (Crespo-Blanc et al., 1994; Johnson et al., 1997; Montenat and Ott d'Estevou, 1999; Martínez-Martínez et al., 2002; Augier et al., 2005c). At a

smaller scale, km-scale subdomes have also been identified by Martínez-Martínez et al. (2002). N-S to NNE-SSW sub-domes in the Sierra Nevada have been related to rolling-hinge deformation, while E-W sub-domes in the Sierra de los Filabres have been related to corrugations or horizontal contraction orthogonal to the regional direction of stretching (Augier et al., 2005c).

The Sierra Bédar corresponds to the southeastern flank of the first-order dome (Fig. 1c) (Augier, 2004; Bakker et al., 1989; Martínez-Martínez, 1986), whereas its northeastern flank exposes an insertion of the Ballabona-Cucharón sub-unit (Sanz de Galdeano and Garcia Tortosa, 2002). In the Sierra Bédar, intense extensional shearing under greenschist-facies conditions is expressed at the top of the metamorphic pile (dotted line on the cross-section Fig. 1c, e) between a km-scale orthogneissic body, known as the Lubrin “granite” (Nijhuis, 1964) and an overlying km-scale metacarbonate body. This shear zone has been interpreted as a secondary detachment structure below the Mecina-Filabres detachment. It affects various lithologies of the Bédar-Macael sub-unit such as graphitic schists, serpentinites and metabasites with some remnants of Triassic evaporites and ophites. Metacarbonates are also encountered as decametre to hectometre-scale tectonic boudins frequently associated with iron-ore deposits. At the base, the Bédar-Macael sub-unit is separated from the underlying graphitic schists of the Calar-Alto unit by the El Marchal shear zone (Fig. 1c) (Martínez-Martínez, 1986; Bakker et al., 1989; Augier, 2004). Relics of eclogites in the metabasites record high-grade (550-650 °C, 18-20 kbar) conditions predating greenschist facies (400-500 °C, 3-4 kbar) retrograde metamorphism related to the top-to-the-west extension (Bodinier et al., 1987; Gomez-Pugnaire and Fernandez-Soler, 1987; Puga et al., 2000). The higher metamorphic grades within the Bédar-Macael sub-unit indicate that the El Marchal shear zone is probably a thrust related to the stacking stages of the orogenic wedge. Reactivation of the El Marchal shear zone as a detachment has been inferred from structural models more clearly defined along cross-sections further West (Augier et al., 2005a).

The green biotite in the orthogneiss analysed here was unaffected by the chloritization which is well developed in the overlying graphitic schists, metabasites and serpentinites. Ductile shearing

within the orthogneiss indicates a quite homogeneous top-to-the-west sense of shear (Fig. 1c) (Soto et al., 1990). U/Pb dating of magmatic zircons yields ages of 314 ± 7 Ma (Martínez-Martínez et al., 2010) and 301 ± 7 Ma (Gomez-Pugnaire et al., 2004). The leucogranite protolith of the orthogneiss intruded older Paleozoic rocks that currently correspond to graphitic schists. The Hercynian basement was subsequently covered by Triassic sediments such as marls, evaporites and limestones, whose metamorphic equivalents are now observed within the Bédar-Macael unit (Egeler, 1963). The quartz veins studied here are developed in the orthogneiss. Quartz veins parallel to the foliation (V-par veins, Table 1) are quite ubiquitous while discordant quartz veins (V-dis veins, Table 1) are localized on top of the orthogneissic body within a zone less than 400 m thick below the upper shear-zone (Fig. 1e).

3. Methodology

3.1. Sample preparation and petrography

Conventional thin (30 μm) and doubly polished thick (200 μm) sections were prepared at GeoRessources laboratory (Nancy, France) from representative oriented samples of the host-rocks and quartz veins for petrographic observation and fluid inclusion study, respectively. These sections were cut perpendicular to the foliation and parallel to the lineation. Petrographic observations were carried out using a Zeiss AxioImager.A1m optical microscope.

3.2. Whole-rock geochemistry

Bulk compositions (major and trace elements) were obtained by ICP-OES and ICP-MS spectrometry (LiBO_2 fusion) at the CRPG-CNRS laboratory (Nancy, France). Sample preparation, analytical conditions and limits of detection are given in Carignan et al. (2001).

3.3. Fluid inclusions

3.3.1. Orientation of fluid inclusion planes

Systematic measurements of the orientation (strike and dip) of intragranular fluid inclusion planes were carried out on each section using an ANIMA interactive videographic analyzer adapted for such studies (Lespinasse et al., 2005) at GeoRessources laboratory (Nancy, France).

3.3.2. Microthermometry

Phase transitions in fluid inclusions were characterized at temperatures between $-170\text{ }^{\circ}\text{C}$ and ca. $+400\text{ }^{\circ}\text{C}$ using a LINKAM MDS 600 heating-freezing stage equipped with a CCD camera mounted on an Olympus microscope at GeoRessources laboratory (Nancy, France). Table 2 summarizes the phase transitions observed as well as the abbreviations of terms and temperatures of phase transitions. The microthermometric stage was calibrated using CO_2 and H_2O synthetic fluid inclusion standards for T_e and $T_m(\text{ice})$ and cross-calibrated natural alpine fluid inclusions for $T_m(\text{hl})$ and $T_h(\text{L})$. The accuracy of measurements is estimated at $\pm 0.2\text{ }^{\circ}\text{C}$ for T_e and $T_m(\text{ice})$ (heating at $0.5\text{--}1\text{ }^{\circ}\text{C}/\text{min}$) and $\pm 2\text{ }^{\circ}\text{C}$ for $T_m(\text{hl})$ and $T_h(\text{L})$ (heating at $1\text{--}5\text{ }^{\circ}\text{C}/\text{min}$). The volumetric fraction of the vapour phase at room temperature was determined optically. Even if KCl is present in large amounts as shown by LAICPMS analyses (see 4.4.), the fluid inclusion composition was calculated in the $\text{H}_2\text{O}\text{--}\text{NaCl}\text{--}\text{CaCl}_2$ system using $T_m(\text{ice}) - T_m(\text{hl})$ pairs using data from Steele-MacInnis et al. (2011). The reason is that no sylvite daughter mineral was observed at room temperature in the aqueous phase (Bodnar, 2003). This is a simplified view of the fluid inclusion composition, however, according to the topography of $\text{H}_2\text{O}\text{--}\text{NaCl}\text{--}\text{KCl}$ and $\text{H}_2\text{O}\text{--}\text{NaCl}\text{--}\text{CaCl}_2$ systems, reconstitution of the total salinity will be relatively unaffected. The isochores were reconstructed

according to the empirical equation of state of Zhang & Frantz (1987), which is used within a PT domain of validity of T : 180-700 °C and P : 0.1-300 MPa.

3.3.3. Raman spectroscopy

Raman analysis of fluid inclusions (vapour and solid phases) was performed with a LabRAM microspectrometer (Horiba Jobin Yvon) equipped with a 1800 gr.mm^{-1} grating and a $\times 80$ objective (Olympus) at GeoRessources laboratory (Nancy, France). The exciting radiation was provided by an Ar^+ laser (Stabilite 2017, Newport Corp., Spectra Physics) at 514.5 nm with a power of 400 mW. Signal-to-noise ratio was optimized by adjusting the acquisition time and accumulation number. Quantitative analysis of the gas phase was performed using a specific calibration in the laboratory (Dubessy et al., 1989). Gas concentrations are given as mol% relative to the sum of other gases (here CO_2 and N_2) in the vapour phase at room temperature (i.e. H_2O vapour is not included in this calculation).

3.3.4. LA-ICP-MS

Individual fluid inclusions on one sample of each type of veins (V-par and V-dis) were ablated and analysed for their detailed element concentration by LA-ICP-MS at GeoRessources laboratory (Nancy, France) (Leisen et al., 2012a). The laser ablation-inductively coupled plasma mass spectrometry (LA-ICP-MS) system is composed of: (1) a GeoLas excimer laser (ArF , 193 nm, Microlas, Göttingen, Germany); (2) an optical microscope (Olympus BX41) for sample observation and focusing the laser beam onto the sample and (3) an Agilent 7500c quadrupole ICP-MS. The sample is located inside a 24.5 cm^3 cylindrical ablation cell, attached to a motorized X–Y stage of the optical microscope. The laser beam is focused onto the sample with a Schwarzschild reflective objective (magnification 25 \times ; numerical aperture = 0.4). Samples are observed using the

microscope equipped with a glass objective (10×, 15×) or a Schwarzschild objective (25×), with a CCD camera attached to the microscope. Sample observation is possible during the ablation. To reduce elemental fractionation (Gunther and Heinrich, 1999), the ablated material is entrained in helium gas (0.5 L min^{-1}) mixed with argon via a cyclone mixer (volume of 9.5 cm^3) prior to entering the ICP torch. The recorded isotopes were ^7Li , ^{23}Na , ^{24}Mg , ^{29}Si , ^{39}K , ^{43}Ca , ^{57}Fe , ^{63}Cu , ^{66}Zn , ^{88}Sr and ^{137}Ba and ^{208}Pb . Calibration and signal integration were performed using the NIST SRM 610, 612, 614 synthetic glasses as reference materials (Pearce et al., 1997) and the LASP software (Leisen, 2011). Absolute elemental concentrations were calculated using the charge-balance technique (Allan et al., 2005), based on a chlorinity of 5.1 mol kg^{-1} solution (as derived from the salinity determined from microthermometry expressed in mass% $\text{NaCl} + \text{CaCl}_2 \text{ eq.}$). The detection limits were calculated using the 3σ criterion (Longerich et al., 1996). Absolute elemental concentrations are given in ppm and uncertainties range from 10 to 30 % for major elements (Na, Ca, K and Mg) and from 30 to 50% for trace elements (Li, Pb, Fe, Cu, Zn, Sr, Ba and Pb) (Leisen et al., 2012a). Cl/Br ratios were also determined independently in a series of representative fluid inclusions using the specific procedure described by Leisen et al. (2012b). Cl/Br ratios are quoted with an uncertainty of 30%.

3.3.5. Crush-Leach

Cl and Br concentrations of bulk fluid inclusion populations were determined using the bulk crush-leach technique (Banks et al., 2000). Quartz veins were crushed to a grain size of 1-2 mm. Pure mineral separates were then picked under a binocular microscope and placed in an ultrasonic bath for 1 hour. Then, samples were cleaned by boiling twice in double distilled water. Cleaned quartz grains (0.5 and 1.0 g) were then crushed to a fine powder in an agate pestle and mortar and leached in 5-6 ml of double distilled water. Leachates from fluid inclusions were analysed for Cl and Br with an ICS 3000 Dionex with column AS20 at LIEC laboratory (Nancy, France). Molar

Cl/Br ratios are quoted with an error of less than ± 5 % based on duplicate analyses of the samples and the replicate analysis of a standard sample.

3.4. Stable isotopes ($\delta^{18}\text{O}$, δD) of fluid phase and minerals

3.4.1. $\delta^{18}\text{O}$ of quartz

The oxygen isotope composition of quartz was analysed at the Géosciences stable isotope laboratory (University of Rennes 1, France). Pure quartz grains were separated by handpicking under a binocular microscope and ground in a boron carbide mortar. To remove O_2 from quartz, about 6-7 mg of quartz powder were reacted overnight with BrF_5 at 670°C using the methodology of Clayton and Mayeda (1963). O_2 was then converted into CO_2 by reaction with hot graphite. CO_2 was analysed isotopically using a VG SIRA 10 triple collector mass spectrometer. Values of $\delta^{18}\text{O}$ for quartz are reported in standard per mil (‰) notation relative to SMOW (Standard Mean Ocean Water). The measured $\delta^{18}\text{O}$ values were slightly corrected given the specific value obtained on the NBS28 international standard and the in-house A1113 granite standard. The amplitude of the $\delta^{18}\text{O}$ correction was less than 0.5 ‰. Taking into account standard correction and internal reproducibility, the analytical uncertainty for quartz $\delta^{18}\text{O}$ values is ± 0.2 ‰ (1 σ). For quartz containing intragranular fluid inclusions planes, $\delta^{18}\text{O}$ of the aqueous fluid is calculated from the value of $\delta^{18}\text{O}_{\text{quartz}}$ and the equilibrium fractionation between quartz and water (Zheng, 1993) considering the temperature of quartz precipitation derived from microthermometry.

3.4.2. δD of white micas

Analyses of the hydrogen isotope composition of white micas from the orthogneiss and from schist layers intercalated within the gneiss were carried out at the CRPG-CNRS laboratory (Nancy,

France) using an Eurovector Elemental Analyzer (EA) coupled to a VG Isoprime Isotope Ratio Mass Spectrometer (IRMS), following the procedure described in Lupker et al. (2012). Between 2 and 8 mg of powdered samples were loaded into tin capsules and degassed at 120 °C under vacuum for 48 h in a degassing canister to remove adsorbed water. After dehydration, samples were transferred under a N₂ dry atmosphere in a customized, sealed, automatic sampler pre-flushed with He in order to avoid any contact with atmospheric moisture. This sampler was then connected to the EA-IRMS system. Samples were combusted at 1450 °C on an EA glassy carbon reaction tube, filled with glassy carbon chips, leading to the reduction of hydroxyl groups to H₂. The produced gases were separated on a chromatographic column. The recovered H₂ was introduced in the IRMS source and analysed for hydrogen isotope composition. Three different internal standards (Muscovite: MuscD65, Phlogopite: Mica-Mg and a fine grained marine sediment from the Bay of Bengal: SO188) were routinely included during the sample analyses. Values of δD are reported in standard per mil (‰) notation relative to SMOW (Standard Mean Ocean Water). The overall, long term, 1 σ , reproducibility of the method on silicate powders is given at 2 ‰ for δD .

3.4.3. δD of fluid inclusions

The hydrogen isotope compositions of bulk fluid inclusions in quartz veins were analysed at the CRPG-CNRS laboratory (Nancy, France). Quartz veins were crushed to a grain size of 1-5 mm and separated by handpicking under the binocular microscope to avoid mineral impurities. Quartz grains were then heated at 100 °C overnight to remove atmospheric water before analyses. 1-3 g of quartz grains were crushed in stainless steel tubes under vacuum at 110 °C. The liberated H₂O and CO₂ were collected in a liquid nitrogen cold trap and non-condensable volatiles (e.g. N₂) were evacuated. To separate CO₂ from H₂O, the liquid nitrogen trap was replaced by an alcohol + liquid nitrogen slush trap at -80 °C. The liberated CO₂ was trapped in a liquid nitrogen cold trap and the amount of recovered CO₂ measured in a calibrated volume using a Keller manometer. However,

CO₂ was never in sufficient amount to be analysed, and was thus removed from the system. Water was liberated from the -80 °C trap and passed through a U furnace at 800 °C, where H₂O was reduced to H₂. H₂ was then pumped using a Toepler pump. The recovery of H₂ from H₂O is assumed to be 100 %. The amount of H₂ was measured in a calibrated volume using a Keller manometer. The H₂ was then extracted and analysed isotopically using a dual-inlet VG Micromass 602D mass spectrometer. Values of δD for H₂, and thus also for the H₂O in fluid inclusions, are reported in standard per mil (‰) notation relative to SMOW. When introduced into the same vacuum line with a vacuum-tight micro-syringe, values for the ED3 standard (-60 ‰) were reproduced to within ± 3 ‰ (2σ). Because water adheres to the internal surfaces of the vacuum system, H isotope analysis is subject to a memory effect, whereby the measured δD value of a sample is shifted from its true value towards the δD value of the previous samples. Memory effects are most pronounced when consecutive samples have substantially different isotopic compositions, as well as when the amount of water reduced in the reactor is significantly different. To avoid this problem, samples were systematically duplicated, and the δD deviation between each isotopic measurement was less than ± 1.5 ‰. For each duplicate, δD values from the first extraction were thus not considered, since it was potentially affected by this memory effect. Taking into account the overall reproducibility of internal standards and sample duplicates, δD values are quoted with a precision better than 3 ‰.

4. Results

4.1. Lithology, structural analysis and petrography

The orthogneiss is mainly composed of quartz, green biotite, white micas and feldspar. This lithology can be intercalated with micaschist layers and locally shows concentrations of syntectonic tourmaline. The average foliation is presented for each sampling site (Fig. 1d). The average dip of

the foliation is around 45° but can reach up to 75° at site 3. The stretching lineation as picked out by tourmaline crystals is relatively constant around WNW-ESE (Fig. 1c, 2, 3c). The orthogneiss can be locally folded with fold axes parallel to the stretching lineation, indicative of corrugation features (Fig. 2).

Two main types of quartz veins are observed (V-par and V-dis; Fig. 2, 3a-c, Table 1). V-par are parallel to the host-rock foliation (Fig. 2 a-c). V-dis are discordant to the host-rock foliation (Fig. 2) and perpendicular to the stretching lineation (Fig. 2c). V-par and V-dis are not boudinaged but can be locally folded as corrugation features (Fig. 2b, c). V-par show a maximum thickness of less than 10 cm. These veins attain lengths of more than several metres, and can be composed of translucent (Fig. 3a, b) or milky quartz (Fig. 3b) and may contain tourmaline crystals and micas. In milky V-par, the mica flakes are parallel to the vein walls (Fig. 3f3). In translucent V-par, a characteristic is that some quartz *c*-axes are oriented perpendicular to the vein walls (Fig. 3e). V-dis are up to several decimetres long and a few centimetres wide, with very few examples of metre-scale veins showing opening at least 10 cm wide. V-dis are developed within the gneiss and generally vertically interrupted by micaschist layers (Fig. 2d) or may cut the micaschist layers when associated with normal displacement (Fig. 2e). V-dis only contain translucent quartz (Fig. 3b-d, f). V-dis are usually lenticular shaped, indicative of tension gashes confined within the gneiss (Fig. 3c). These veins may also abut against the contact with thickest micaschist layers or at the contact with translucent V-par (Fig. 3f2). V-dis may displace milky V-par. This is even more noticeable where the opening is associated with normal faulting (Fig. 3b).

Crosscutting relationships between these two types of veins show that V-dis postdate V-par milky quartz veins especially when associated with normal faulting (Fig. 3b). However, in some cases, at the contact between the two veins, the quartz crystals show a diffuse contact. In the example illustrated by Fig. 3f, V-dis vein with large quartz crystals terminates with a blurry contact in a V-par milky quartz vein characterized by much smaller grains (Fig. 3f2). In one particular example (Fig. 2b), a translucent V-par is folded as ridge and furrow (i.e. corrugation) with an axis

parallel to the stretching lineation. V-dis is perpendicular to the fold axis and mineral lineation developed on top of the ridge. V-dis is branched on the folded V-par and ends about 20 cm upward. This geometry and the diffuse contact between V-par and V-dis suggest a relationship between the folding of V-par and the opening of V-dis in relation with the top to the WNW shearing.

Frequently, a halo of bleached orthogneiss reaching several centimeters is observed around V-dis (Fig. 3c) but rarely (or with a very limited extension) around V-par. This bleaching tends to disappear at the vein tip or may be heterogeneous and developed only on one side of the V-dis (irregular alteration halo on Fig. 3c). The absence of white mica and green biotite as well as the formation of xenomorphic rutile are characteristic of the bleached zone. This feature is also reflected by the whole-rock geochemistry (Table 3) that reveals a decrease of Fe_2O_3 and K_2O in the bleached zone. At the wall of V-dis, newly recrystallized green biotite is developed parallel to the wall as well as pyrite crystals. Some fractures devoid of quartz may reveal a similar halo and contain some pyrite crystals. Trace element distributions also show more or less pronounced differences between both zones. In particular noticeable depletion in Ba, Cs, Rb, Sn and Zn and enrichment in Co, Cu and Sr are observed in the bleached zone compared to the unaltered orthogneiss (Table 3).

Two types of quartz grains are recognized in both V-par and V-dis. These veins display a heterogeneous microstructure with porphyroblast quartz crystals, remnants of primary centimetre-size grains, designated as Q_{rem} . They might be surrounded by recrystallized grains with variable size and devoid of fluid inclusions, defined as Q_{xt} . Q_{rem} grains show undulatory extinction and the presence of subgrain boundaries. The Q_{rem} grains present in V-dis are on average five times larger than in V-par, and are not preferentially oriented (Fig. 3d-f). Quartz in V-par can be either milky or translucent. In the case of milky quartz veins, the vein walls are not clearly defined. Q_{rem} grains frequently display 120° triple junctions (Fig. 3g). Mica flakes are oriented parallel to the foliation (Fig. 3f3). Recrystallized quartz grains are observed (Fig. 3f). Local shear planes illustrated by oriented quartz grains can be observed at some grain boundaries, indicating ongoing localized

ductile deformation (Fig. 3f-h). The walls of V-par with translucent quartz are more clearly defined (Fig. 3a). Mica flakes are randomly oriented. The largest grains Q_{rem} show the c -axis of the quartz crystals perpendicular to the vein walls (Fig. 3e). This indicates quartz growth normal to the foliation without any subsequent ductile shearing. In these translucent V-par, Q_{rem} is locally affected by the dynamic recrystallization that generated the Q_{rxt} quartz grains. This population of Q_{rxt} appears as 5-100 μm -sized elongated subgrains mantling larger Q_{rem} grain cores. Two sub-types of Q_{rxt} grains can be identified: $Q_{rxt(1)}$ grains formed by bulging recrystallization (BLG) (present in V-par and V-dis), indicating temperatures of $\sim 300\text{-}400$ $^{\circ}\text{C}$, and frequently displaying 120° angles (Fig. 3g, h); $Q_{rxt(2)}$ grains formed by subgrain rotation (SGR) only observed in V-par, indicating temperatures of $\sim 400\text{-}500$ $^{\circ}\text{C}$ (Urai et al., 1986; Stipp et al., 2002; Passchier and Trouw, 2005). The latter sub-type is sigmoid-shaped, indicating top-to-the-west ductile shearing (Fig. 3g, h), and is aligned parallel to the foliation.

4.2. Fluid inclusion petrography

In Q_{rem} from V-par and V-dis, the fluid inclusions are arranged as fluid inclusion planes (FIPs) that do not intersect the grain boundaries (i.e. intragranular planes) but extend from grain boundary to grain boundary (Fig. 3d, 4a). In V-par and V-dis, FIPs are always parallel at the scale of individual grains. Considering their overall distribution, they seem to show two preferential orientations for each V-par and V-dis defining two sets of poles with an acute angle of approximately 60° between them (pole projections Fig. 4c). In V-par, intragranular FIPs in Q_{rem} grains are well preserved except in the vicinity of $Q_{rxt(2)}$ grains.

In intragranular FIPs from both V-dis and V-par, fluid inclusions are composed of a liquid, a vapour and a daughter halite NaCl phase at room temperature. Other mineral phases like calcite have been episodically identified by Raman spectrometry (Fig. 4d). Optical estimation of the volumetric fraction of vapour phase yields 20-25 vol.%. These fluid inclusions are generally larger

than 15 μm , and some of them can reach more than 30 μm in diameter. Within a single intragranular FIP, the inclusion shapes can vary from slightly irregular to crystal-negative (euhedral) in the two sets of veins (Fig. 3i, 4).

In both V-par and V-dis, no transgranular FIPs (i.e. secondary fluid inclusion planes) are observed. Furthermore, there seems to be no isolated or clustered fluid inclusions. Q_{rxl} grains are devoid of fluid inclusions.

4.3. Microthermometric characteristics of fluid inclusions

The observed eutectic temperatures (T_e) range from -75 to -35 $^{\circ}\text{C}$. This range indicates a complex salt system with other components than NaCl including divalent cations. Consequently the salinity was approximated in the ternary H_2O -NaCl- CaCl_2 system. No clathrate was observed, indicating that the vapour phase has a low density. Ice melting temperatures $T_{\text{m(ice)}}$ range between -38 and -18 $^{\circ}\text{C}$ for V-par and between -43 and -19 $^{\circ}\text{C}$ for V-dis (Table 4). Halite dissolution temperature $T_{\text{m(hl)}}$ in the presence of vapour, ranges from 130 to 240 $^{\circ}\text{C}$ for V-par and from 160 to 280 $^{\circ}\text{C}$ for V-dis (Table 4). $T_{\text{h(L)}}$ values are between 210 and 365 $^{\circ}\text{C}$ (mode: 330 $^{\circ}\text{C}$) for V-par (Fig. 5, Table 4) and between 220 and 400 $^{\circ}\text{C}$ for V-dis with a mode at 280 $^{\circ}\text{C}$ significantly lower than for V-par (Fig. 5). The highest values of T_{h} for V-par and V-dis are values obtained with deformed inclusions (Fig. 5). The most deformed inclusions, as indicated by their shape and corresponding higher homogenization temperatures are not considered any further. The salinity reconstructed from $T_{\text{m(hl)}} - T_{\text{m(ice)}}$ pairs is comprised between 29.7 and 37.6 mass% NaCl + CaCl_2 for V-par and between 30.8 and 41.3 mass% NaCl + CaCl_2 for V-dis (Fig. 5, 6).

4.4. Detailed composition of fluid inclusions

Raman spectrometry analyses show that the vapour phase of fluid inclusions is characterized by traces of CO₂ and N₂ in relative proportions varying between 0-40 mol% N₂ and 60-100 mol% CO₂ for V-par and 0-20 mol% N₂ and 80-100 mol% CO₂ for V-dis (Table 4).

Table 5 and Fig. 7 report the Cl/Br molar ratios and mean Cl concentrations derived from the salinity as expressed in mass% NaCl + CaCl₂ as determined from microthermometry for fluid inclusions from V-par and V-dis. The mean chlorinity is between 5000 and 5700 mmol/kg solution for inclusions from V-par and between 4700 and 6100 mmol/kg solution for inclusions from V-dis. Cl/Br molar ratios determined by crush-leach analysis are between 295 and 990 for inclusions from V-par and between 170 and 1475 for inclusions from V-dis. Cl/Br molar ratios determined by LA-ICP-MS analysis are between 310-2400 for inclusions from V-par and between 210 and 4500 for inclusions from V-dis. No significant difference in the Cl/Br ratios can be observed between the two methods, with the exception of 8 out of 30 Cl/Br values determined by LA-ICP-MS between 2000 and 4400. Note that crush-leach data represent average composition of bulk fluid inclusion populations and that it is therefore expected that halogen composition of individual fluid inclusions as determined by LA-ICP-MS show dispersion around the average values for each sample (Leisen et al. 2012b). Moreover, for the samples where both crush-leach and LA-ICP-MS data were acquired, the Cl/Br ratios obtained by crush-leach fall systematically within the range of values determined by LA-ICP-MS.

The detailed cationic compositions of fluid inclusions for each type of vein are shown in Table 6 and Fig. 8 as elemental concentrations (in ppm). Fluid inclusions in V-par (15 analysed fluid inclusions) and V-dis (6 analysed fluid inclusions) are most generally dominated by Na (41000-80000 ppm and 69000-81000 ppm respectively). Na is therefore more concentrated on average in V-dis compared to V-par inclusions. Then, by decreasing concentration, K, Ca, Mg and Fe are broadly similar in both V-par and V-dis inclusions (14000-45000 ppm, 8100-24000 ppm, 3500-19000 ppm and 2800-15000 ppm, respectively). Sr and Li show significantly higher concentrations in most fluid inclusions from V-par compared to V-dis (Sr: 650-2600 ppm and 630-660 ppm,

respectively; Li: 580-1700 ppm and <110 ppm, respectively). Given the number of data showing concentrations below limits of detection, Cu, Zn, Ba and Pb concentrations cannot be reasonably distinguished between inclusions from V-par and V-dis. Concentrations above the limits of detection for Cu, Zn, Ba and Pb are 220-1200 ppm (3 data), 380-1090 ppm (16 data), 240-3400 ppm (12 data) and 140-530 ppm (15 data), respectively.

4.5. O and H isotopes in quartz, white mica and fluid inclusions

The $\delta^{18}\text{O}$ values of quartz from the orthogneiss range between 17.8 ± 0.5 and 18.7 ± 0.5 ‰ (Table 7). $\delta^{18}\text{O}$ values for the vein quartz range from 12.6 ± 0.5 to 13.8 ± 0.5 ‰ for V-par and from 13.4 ± 0.5 to 15.4 ± 0.5 ‰ for V-dis (Table 7). The δD values of the water trapped in fluid inclusions within quartz veins, range between -39.8 ± 3 and -27.8 ± 3 ‰ for V-par and between -32.8 ± 3 and -16.7 ± 3 ‰ for V-dis (Table 7). δD values for white micas from intercalated layers of schist are in the range -99 ± 2 to -101 ± 2 ‰. The δD values of white micas from the orthogneiss range from -35.4 ± 2 to -45.6 ± 2 ‰ (Table 7).

5. Discussion

5.1. Tectonic conditions of vein formation and fluid trapping

The geometry and also the orientation of mica flakes within milky V-par would argue for vein transposition during the ductile shearing (Fig. 3f3). However, in the translucent quartz vein (Fig. 3a), the presence of quartz *c*-axes developed perpendicularly to the vein walls (Fig. 3e) seems incompatible with a complete ductile transposition. The absence of partly transposed veins revealing intermediate stages of ductile deformation suggests that V-par translucent veins formed from fluids injected parallel to the foliation. A folded V-par translucent vein displays a decimetre-

scale ridge and furrow morphology. Fold axes are parallel to the host-rock lineation. V-dis perpendicular to the foliation and to the lineation are branched on top of this V-par folded vein. These folds can be interpreted as corrugation features related to the top-to-the WNW shearing where associated V-dis correspond to the last stages of deformation under more brittle conditions. As an alternative explanation, these folds may also correspond to a horizontal shortening perpendicular to the lineation just prior to the branching of V-dis.

Although structural and petrographic observations suggest that V-par translucent veins directly formed parallel to the foliation, the interpretation regarding their formation is not straightforward. One explanation could be the occurrence of a local compressional regime with horizontal Z and vertical X axes developed in an intrado position within a larger scale E-W dome structure forming while the orthogneiss was deforming at the ductile-brittle transition. Another explanation could be the occurrence of fluid overpressure in relation with a decrease of the vertical load during rapid exhumation stages that would have permitted fluid injections within the foliation. Both explanations could even be complementary.

Within a single quartz grain, intragranular fluid inclusion planes are oriented parallel to each other. However, considering their overall distribution, they seem to show two preferential orientations (pole projections of Fig. 4). Their formation is not the result of regional stress under brittle conditions as no transgranular planes are observed. Due to the many clues that quartz was undergoing ductile deformation and dynamic recrystallization during vein opening, intragranular FIPs are thus interpreted as the result of fluid entrapment along surfaces showing preferential crystallographic orientation (Van Den Kerkhof and Hein, 2001). The entrapped fluid can be issued from earlier fluid inclusions that reequilibrated along specific crystallographic planes during quartz plastic deformation (Tarantola et al., 2010, 2012; Diamond and Tarantola, 2015; Stünitz et al., 2017). Alternatively it can represent a fluid wetting grain boundaries that is trapped along crystallographic planes that would open by local stress during plastic deformation (Siebenaller et al., 2016). Here, the lack of isolated primary fluid inclusions, together with the homogeneous fluid

inclusion population observed suggest that the fluid inclusions are representative of the fluid involved with vein opening and simultaneous plastic deformation. At the *PT* conditions of vein formation and fluid entrapment, FIPs with two dominant orientations are open, corresponding to more active crystallographic planes at these conditions (Stipp et al., 2002). Moreover, as demonstrated by the presence of planes containing deformed fluid inclusions, dynamic recrystallization of quartz host-crystals still takes place after fluid entrapment.

The presence of intragranular FIPs and the lack of transgranular FIPs indicate that fluid trapping predates complete brittle conditions. These intragranular planes were obliterated at the contact with Q_{rt} grains due to SGR recrystallization in the translucent quartz veins. The sigmoidal-shaped $Q_{\text{rt}(2)}$ grains (Fig. 3h) also demonstrate a relation with the regional top-to-the-west shearing which postdates the fluid trapping in V-par translucent vein. Geometric relations show that V-dis postdate V-par but their contact is not straight but rather diffuse (Fig. 3f2). At the microscopic scale, feldspars are clearly cut at the contact with V-dis quartz grains (Fig. 3f1). As a consequence, there must be a continuous evolution from V-par to V-dis vein setting from ductile to ductile-brittle conditions during westward shearing of the orthogneiss.

5.2. *PT* conditions of fluid circulation

In the absence of any index mineral within the gneissic host-rock, *PT* conditions of fluid circulation and vein formation can solely be constrained by the intersection of the isochores of fluid inclusions and temperatures derived from microstructural observations. Tullis and Yund (1987) show that feldspar deforms under purely brittle conditions, while the quartz shows intracrystalline deformation and ductile recrystallization in a large range of temperature below around 600 °C as a function of the strain rate. The ductile-brittle transition of quartz is in the range 250-400 °C, while that of feldspar is in the range 400-600 °C. According to the structural observations between V-par and V-dis and feldspar and quartz microstructural deformation features, vein formation might be in

the range 400-600 °C for V-par (BLG + SGR recrystallization of quartz) while V-dis (BLG recrystallization of quartz and brittle deformation of feldspar) would likely form when temperatures are lower than about 250-400 °C. The upper temperature limit of 600 °C for V-par trapping can also be constrained by the regional metamorphic conditions inferred for the evolution of the MCC by De Jong (1992) and Augier et al. (2005a) (Fig. 10).

The isochores of fluid inclusions for both V-par and V-dis (Fig. 10a-b) show a large variability that can be explained either as (1) reflecting continuous fluid entrapment with varying *PT* conditions and/or (2) by a change of volume of relict fluid inclusions after entrapment (Kerrich, 1976; Sterner and Bodnar, 1989; Diamond et al., 2010). The most deformed inclusions (Fig. 5, 6) are not considered in the representation of the isochores of Fig. 10. During a later stage of decompression associated with exhumation, these fluids could be locally remobilized at the scale of quartz grains within the veins after partial or total decrepitation and formation of neonate inclusions under ductile to brittle deformation conditions. The reequilibration processes of fluid inclusions during decompression could reflect this relatively large range of lower *PT* conditions for both sets of veins. This feature is typical of inclusions that have undergone changes in density after partial leakage (Sterner and Bodnar, 1989; Bakker and Jansen, 1991; Bakker and Jansen, 1994).

Accordingly, the calculated *PT* conditions determined from intersection of isochores with the *PT* path of the Bédar-Macael sub-unit (De Jong, 1992; Augier et al., 2005a) indicate continuous entrapment from 100-560 MPa (the upper conditions are certainly underestimated as it is based on the *VX* properties of the preserved inclusions) at 320-600 °C for V-par fluids to 60-340 MPa at 250-400 °C for V-dis fluids (Fig. 10c-d). These *PT* conditions account for the structural and microstructural observations.

5.3. Origin of the fluids

With few exceptions, δD_{fluid} and $\delta D_{\text{white micas}}$ from the orthogneiss show apparent equilibrium temperatures compatible with the metamorphic conditions experienced by the rocks in a range 400-

600 °C (Table 7). Our analyses preclude isotopic equilibrium of the fluid trapped within V-par and V-dis with intercalated schist layers (Table 7, Fig. 9). Moreover in any case, $\delta^{18}\text{O}_{\text{quartz vein}}$ is different from $\delta^{18}\text{O}_{\text{quartz host-rock}}$ with $\delta^{18}\text{O}$ of V-par slightly lower than that of V-dis (Table 7), thus indicating disequilibrium between veins and host-rock (Oliver, 1996). The only scenario that can fulfil these isotopic observations implies an external fluid with a high fluid/rock ratio permitting isotopic equilibration of white micas of the orthogneiss. The D-depleted values (around -100‰) of the intercalated schist layer likely indicate that they localised circulation of meteoric water in the last stages of exhumation.

Besides oxygen isotopes, a chemical/mineralogical disequilibrium is also shown by the presence of a centimetric bleached zone around the veins. Chemical analyses of both host-rock and the bleached zones indicate element depletion or enrichment. Because no late secondary transgranular fluid inclusion planes were observed and because the orthogneiss and the fluid of the vein are not at chemical/mineralogical and isotopic equilibrium, the bleached area is likely contemporaneous of the vein formation from an external brine. As an alternative explanation, the alteration may also be due to a more recent fluid flow favored by the pre-existing fracture network (Oliver, 1996). Such bleaching zones have also been observed to the South of Bédar along joint networks affecting the orthogneiss but devoid of quartz filling. However, in the absence of thermodynamic calculation at the *PT* conditions of formation, it is not possible to conclude if the enrichment/depletion of the fluid in some elements is entirely controlled by the alteration around the veins.

Three possible origins for the water and the high salt content of fluid inclusions can reasonably be invoked here: (i) exsolution from a magma; (ii) dissolution of evaporites (basinal or metamorphosed) and (iii) evaporation of seawater.

Detailed compositions of the fluids as determined by LA-ICP-MS analyses (Table 6, Fig. 8) may help constrain the origin of the fluids and the fluid-rock interactions that occurred (see Yardley (2005) for a compilation of typical fluid compositions). Here, Na and Ca concentrations are hardly

discriminant between basinal, metamorphic or magmatic fluids. High K concentrations are more typical of magmatic fluids, while high Mg concentrations would rule out a magmatic origin. The relatively high metal contents (Fe, Zn, Ba and Pb) are generally attributed to magmatic fluids although metal-rich basinal or metamorphic brines are not uncommon (Eglinger et al., 2014; Richard et al., 2016). Collectively, the major and trace element compositions of the fluid inclusions are not indicative of a typical basinal, metamorphic or magmatic fluid. However, fluids combining high-temperature and high Cl, Na, Ca, K and Mg content are most frequently attributed to metamorphic brines related to dissolution of metaevaporites (Banks et al., 2000; Eglinger et al., 2014).

Petrographic observations indicate continuous fluid entrapment of a single fluid within quartz veins at ductile to brittle conditions. This discards the possibility of isotopic reequilibration at elevated temperatures by water diffusion due to fugacity gradient by the arrival of a second fluid (Doppler et al., 2013; Bakker, 2017). The analysed δD values of water trapped within fluid inclusions thus represent the nominal signature of the circulating fluid at the time of trapping. Considering the δD_{fluid} values between -39.8 and -16.7 ‰ obtained by crushing techniques and the calculated $\delta^{18}O_{\text{fluid}}$ in the range 4.4 to 11.7 ± 0.5 ‰ considering quartz-fluid equilibrium at 320 - 600 °C for V-par and 250 - 400 °C for V-dis (Table 7), the stable isotope composition of the fluids is compatible with a metamorphic origin and not with a magmatic or basinal origin (Sheppard, 1986; Wilkinson et al., 1995) (Fig. 9).

The high silica content of the orthogneiss (78 wt% SiO_2) might reflect low temperature silicification prior to burial, deformation and recrystallization. This alteration would result in the high $\delta^{18}O$ values around 18 ‰ observed in the orthogneiss, too high to express the original magmatic isotopic signature. Taken together, the stable isotope data indicate that the brines have a metamorphic origin and have undergone protracted interaction with the altered host orthogneiss. However, a fluid source external to the orthogneiss must be invoked since the $\delta^{18}O$ values of the quartz veins and of the orthogneiss are not at equilibrium and the orthogneiss itself can hardly be

considered as a source of fluid, and no metamorphic reaction would explain the formation of aqueous high-salinity fluids.

Contrary to major elements and stable O and H isotopes, halogens are much less affected by fluid-rock interactions, and thus may preserve the original signature of the fluids. In Fig. 7, the Cl/Br and Cl concentration data plot in a compositional field intermediate between halite-saturated evaporated seawater, halite dissolution brine and diluted magmatic brine. Early Miocene magmatic activity has only been described in the Sierra Cabrera to the south-east of the study area (Westra, 1969) (Fig. 2) where a leucogranite dated at 20.4 ± 0.7 Ma (Bellon et al., 1983; Zeck et al., 1989) crosscuts the metamorphic fabric. Other magmatic or volcanic activities in the area are late-Miocene (Lopez Ruiz and Rodriguez Badiola, 1980; Benito et al., 1999; Duggen et al., 2004, 2005; Prelevic et al., 2008) and therefore postdate the exhumation of the Bédar-Macael units and related vein opening (Fig. 10). Taken together with the stable O, H compositions, this indicates that a magmatic origin for the brines can be ruled out. An episode of sedimentation is recognized across the Sierra Nevada, but is not preserved in the eastern Sierra, corresponding to the deposition of the Ciudad Granada Group of late Oligocene–Aquitainian age followed by the Viñuela Group of Burdigalian age (Serrano et al., 2006). These groups are devoid of evaporites and could not have provided evaporitic brines to the vein system. The subsequent basins recognized in the study area are too recent (Tortonian) (Montenat and Ott d'Estevou, 1990) and therefore could not be the source of brines either from dissolution of basinal evaporites or from evaporation of seawater. Together with the stable O and H isotope data, this indicates that a basinal origin for the brines can be ruled out. Finally, to explain the halogen contents, dissolution of metaevaporites in the metamorphic pile by fluids generated from metamorphic reactions is probably the dominant mechanism for acquisition of high salinity (Yardley and Graham, 2002). The dissolved metaevaporites are most probably located within Triassic units (Dyja et al., 2016). Possible candidates as metaevaporite-bearing units could be local (within the Bédar-Macael sub-unit), or within the Ballabona-Cucharón sub-unit which crops out in the northern flank of the Sierra Bédar (Sanz de Galdeano and Garcia

Tortosa, 2002) or more distal (Gómez-Pugnaire et al., 1994; Pérez-López et al., 2012). However, the Cl/Br ratios here are on average not as high as recorded in fluids from Columbian Emeralds, for example, which serve as a reference for typical metaevaporite-dissolution fluids (Banks et al., 2000) and some of the Cl/Br values are below seawater values (i.e. < 650). This implies that the metamorphic fluids were enriched in Br prior to metaevaporite dissolution or that brines derived from metaevaporite dissolution have been later enriched in Br. Here, possible Br sources could be the regionally extensive graphitic schists of the Calar Alto sub-unit or more the local graphitic schists at the contact with the orthogneiss body within the Bédar-Macael sub-unit. Raman spectroscopy analyses of the Calar-Alto graphitic schists indicate that not-well crystallized graphite (carbonaceous matter) is preserved and could have supplied Br to the fluids (Augier et al., 2005b; Dyja et al., 2016).

5.4. Summary and implications

Fig. 11 summarizes the main findings of this study, integrated within the regional frame of the exhumation of the Nevado-Filabride complex, in the internal zones of the Betic Cordillera, during the middle Miocene. The main results and their regional and wider implications are exposed below.

Quartz veins are developed parallel and discordant to the foliation within an orthogneiss body located in the footwall of the Mecina-Filabres detachment separating the Nevado-Filábride from the overlying *HP-LT* Alpujarrides metamorphic nappes. The detachment footwall is composed mainly of gneisses, schists and metacarbonates from the Bédar-Macael sub-unit. Schist and metacarbonate bodies show evidence of ductile deformation while the gneiss is crossing the brittle-ductile transition in the retrograde exhumation path and veins open. The geometry and deformation of veins suggest opening in relation with the top to the WNW shearing.

The analysis of fluid inclusions in the quartz veins reveals the circulation of a high-salinity (30-40 mass% NaCl_{eq.}) brines in the range 250-600 °C and 100 to at least 560 MPa. Halogen and

isotopic signatures indicate that the brines probably originate from the dissolution of Triassic metaevaporites in the Ballabona-Cucharón and/or Bédar Macael sub-units. Evaporite dissolution was caused by relatively Br-enriched metamorphic fluids that interacted with graphitic schists from the Calar-Alto and/or Bédar-Macael sub-units. Brine inclusions, similar in salinity and temperature to those described in this study, have been described in intragranular fluid inclusion planes in synkinematic quartz veins in the Dos Picos extensional detachment, separating the Veleta unit from the Calar Alto unit, close to Fiñana in the Sierra Nevada (Fig. 1) (González-Casado et al., 1995). Similar brine inclusions have also been described in intragranular fluid inclusion planes in sheared quartz veins in graphitic schists from the Calar-Alto unit cropping out in the Sierra Almagrera further to the east (Fig. 1) (Dyja et al., 2016). In this area, halogen and isotopic signatures indicate that quartz veins formed from a deep fluid reservoir of metamorphic brines derived from the dissolution of Triassic evaporites. The occurrence of similar brines trapped in three different places along a ca. 100 km transect, and probably at the same period, indicates that the fluid event investigated here has a regional extension. However, it remains to be determined, what was the driving force for regional fluid flow and whether the circulation of the deep metamorphic fluids at the origin of evaporite dissolution was regionally pervasive or more structurally focused along major shear zones.

The brines described here carry important quantities of metals (Fe, Cu, Zn, Ba, Pb), in comparable concentrations with those from the Sierra Almagrera (Dyja et al., 2016). It could be speculated that these brines have some relation with the numerous Fe +/- Mn-Ba deposits located in the Nevado-Filabride complex (e.g. Torres-Ruiz, 1983, 2006). In the Sierra Almagrera, ore-stage (Fe, Ba) fluids are related with brines issued from dissolution of Messinian evaporites and brines issued from dissolution of Triassic metaevaporites predate the ore stage (Dyja et al., 2016). In the case of the brines described here, it is not possible to clearly relate this fluid event with the deposits. Further fluid inclusion study within the deposits from the Bédar-Macael sub-unit (Fircks, 1906;

Guardiola and Sierra, 1925) would be necessary to determine whether evaporitic brines were involved in the deposits.

The intersection between the fluid inclusion isochores and the PTt path admitted for the area (De Jong, 1992; Augier et al. 2005a) implies continuous fluid entrapment during exhumation path. Dating of syntectonic phengites related to top to the west shearing indicates that the Bédar-Macael sub-unit passed through the DBT during the Langhian (14 Ma) (Augier et al., 2005a). By extrapolation, vein formation can be also assigned Langhian in age.

The studied vein set underlines brittle deformation at the top of the orthogneiss body in the footwall of the detachment systems, in relation with the regional extensional tectonics. However, in spite of the brittle deformations observed at the outcrop scale, the ubiquitous presence of metamorphic brines in the fluid inclusions and the lack of evidence for trapping of surface-derived fluids, suggests that the deep fluid reservoir was not connected to the hydrosphere reservoir. This separation from the surficial fluid reservoir probably resulted from the presence of an overlying cap of schists and marbles still affected by ductile shearing prior to reaching their specific DBT conditions. This cap would have acted as an impermeable barrier impeding surficial fluids to penetrate below the DBT and reach the orthogneiss level. The downward percolation of surficial fluids below the DBT is usually limited by a dramatic decrease of permeability (Ingebritsen and Manning, 2002; Manning and Ingebritsen, 1999). While surface-derived fluids may cross the DBT and reach the ductile crust in some cases (e.g. Kerrich et al., 1984; Wickham et al., 1993; Morrison, 1994; Upton et al., 1995; Ingebritsen and Manning, 1999; Famin et al., 2004, 2005; Siebenaller et al., 2013; Menzies et al., 2014, 2016; Dyja et al., 2016) it is clearly not the case here, even though local brittle conditions have prevailed in the detachment footwall. The position of the DBT is lithology-specific (Brace and Kohlstedt, 1980; Kohlstedt et al., 1995). Here, local brittle conditions in the orthogneiss within a unit of ductile lithologies were not sufficient to allow surficial fluids to penetrate the detachment footwall. Therefore, during the exhumation of the lithologically and rheologically diverse Bédar-Macael sub-unit, the early stage of crossing of the DBT was not

characterized by a connection between surficial and deep fluid reservoirs and it could be considered that the DBT acted effectively as a hydrological barrier preventing surficial fluids penetration.

Acknowledgments

The authors thank M.-C. Caumon (GeoRessources, Vandœuvre-lès-Nancy) for Raman spectroscopy analyses and T. Rigaudier (CRPG, Vandœuvre-lès-Nancy) for isotopic analyses. We also thank A. Flammang and C. Demeurie who prepared thin and thick sections. The authors also thank Michael Carpenter for his English language review. We are very grateful to P. Agard for editorial handling and A. Verlaquet and R. Augier for their helpful and constructive comments. This work was supported by the Ministry of Higher Education and Research (MESR, France) and the CNRS ST-INSU-CT5 programme.

References

- Allan, M.M., Yardley, B.W.D., Forbes, L.J., Shmulovich K.I., Banks, D.A. and Shepherd, T.J., 2005. Validation of LA-ICPMS fluid inclusion analysis with synthetic fluid inclusions. *American Mineralogist*, 90(11-12): 1767-1775.
- Augier, R., 2004. Evolution tardi-orogénique des Cordillères bétiques (Espagne): Apports d'une étude intégrée. PhD Thesis, Université de Pierre et Marie Curie, Paris 6, 400 pp.
- Augier, R., Agard, P., Monié, P., Jolivet, L., Robin, C. and Booth-Rea, G., 2005a. Exhumation, doming and slab retreat in the Betic Cordillera (SE Spain): In situ $^{40}\text{Ar}/^{39}\text{Ar}$ ages and P-T-d-t paths for the Nevado-Filabride complex. *Journal of Metamorphic Geology*, 23(5): 357-381.
- Augier, R., Booth-Rea, G., Agard, P., Martinez-Martinez, J.M., Jolivet, L. and Azañon, J.M., 2005b. Exhumation constraints for the lower Nevado-Filabride Complex (Betic Cordillera,

- SE Spain): a Raman thermometry and Tweeku multiequilibrium thermobarometry approach. *Bulletin de la Société Géologique de France*, 176(5): 403-416.
- Augier, R., Jolivet, L. and Robin, C., 2005c. Late Orogenic doming in the eastern Betic Cordilleras: Final exhumation of the Nevado-Filabride complex and its relation to basin genesis. *Tectonics*, 24(4): 1-19.
- Bakker, H.E., Jong, K.D., Helmers, H. and Biermann, C., 1989. The geodynamic evolution of the Internal Zone of the Betic Cordilleras (south-east Spain): a model based on structural analysis and geothermobarometry. *Journal of Metamorphic Geology*, 7(3): 359-381.
- Bakker, R.J., 2017. Re-equilibration processes in fluid inclusion assemblages. *Minerals*, 7: 117; doi:10.3390/min7070117.
- Bakker, R.J. and Jansen, J.B.H., 1991. Experimental post-entrapment water loss from synthetic CO₂-H₂O inclusions in natural quartz. *Geochimica et Cosmochimica Acta*, 55: 2215-2230.
- Bakker, R.J. and Jansen, J.B.H., 1994. A mechanism for preferential H₂O leakage from fluid inclusions in quartz, based on TEM observations. *Contributions to Mineralogy and Petrology*, 116: 7-20.
- Banks, D.A., Giuliani, G., Yardley, B.W.D. and Cheilletz, A., 2000. Emerald mineralisation in Colombia: fluid chemistry and the role of brine mixing. *Mineralium Deposita*, 35(8): 699-713.
- Bellon, H., Bordet, P. and Montenat, C., 1983. Chronologie du magmatisme néogène des Cordillères bétiques (Espagne méridionale). *Bulletin de la Société Géologique de France*, 25: 205-217.
- Benito, R., López-Ruiz, J., Cebriá, J.M., Hertogen, J., Doblás, M., Oyarzun, R. and Demaiffe, D., 1999. Sr and O isotope constraints on source and crustal contamination in the high-K calc-alkaline and shoshonitic neogene volcanic rocks of SE Spain. *Lithos*, 46(4): 773-802.

- Bodinier, J.L., Morten, L., Puga, E. and Diaz de Federico, A., 1987. Geochemistry of metabasites from the Nevado-Filabride complex, betic cordilleras, Spain: Relics of a dismembered ophiolitic sequence. *Lithos*, 20(3): 235-245.
- Bodnar, R.J., 2003. Introduction to aqueous-electrolyte fluid inclusions. In: Samson, I., Anderson, A., Marshall, D. (Eds.), *Fluid Inclusions: Analysis and Interpretation*. Mineralogical Association of Canada Short Course Series 32, pp. 81–100.
- Böhlke, J.K. and Irwin, J.J., 1992. Laser microprobe analyses of Cl, Br, I, and K in fluid inclusions: Implications for sources of salinity in some ancient hydrothermal fluids. *Geochimica et Cosmochimica Acta*, 56(1): 203-225.
- Brace, W.F., Kohlstedt, D.L., 1980. Limits on lithospheric stress imposed by laboratory experiments. *J. Geophys. Res.*, 85: 6248-6252.
- Brun, J.P., Sokoutis, D., Van Den Driessche, J., 1994. Analogue modeling of detachment fault systems and core complexes. *Geology*, 22: 319-322.
- Carignan, J., Hild, P., Mévelle, G., Morel, J. and Yeghicheyan, D., 2001. Routine analyses of trace elements in geological samples using flow injection and low pressure on-line liquid chromatography coupled to ICP-MS: a study of reference materials BR, DR-N, UB-N, AN-G and GH. *Geostandards Newsletter* 25: 187-198.
- Clayton, R.N. and Mayeda, T.K., 1963. The use of bromine pentafluoride in the extraction of oxygen from oxides and silicates for isotopic analysis. *Geochimica et Cosmochimica Acta*, 27(1): 43-52.
- Crespo-Blanc, A., Orozco, M. and Garcia-Dueñas, V., 1994. Extension versus compression during the Miocene tectonic evolution of the Betic chain. Late folding of normal fault systems. *Tectonics*, 13(1): 78-88.
- Davies, G.A., Lister, G.S., Reynolds, S.J., 1986. Structural evolution of the Whipple and South mountains shear zones, southwestern United States. *Geology*, 14: 7-10.

- De Jong, K., 1992. A new Geodynamic Model for the Betic Cordilleras based on P-T-t paths and Structural data from the Eastern Betic. *Física de la Tierra*, 4: 77-107.
- Dewey, J.F., Helman, M.L., Knott, S.D., Turco, E., Hutton, D.H.W., 1989, Kinematics of the western Mediterranean Geological Society, London, 45, 265-283, DOI: 10.1144/GSL.SP.1989.045.01.15
- Diamond, L., Tarantola, A. and Stünitz, H., 2010. Modification of fluid inclusions in quartz by deviatoric stress. II: experimentally induced changes in inclusion volume and composition. *Contributions to Mineralogy and Petrology*, 160(6): 845-864.
- Diamond, L.W. and Tarantola, A., 2015. Interpretation of fluid inclusions in quartz deformed by weak ductile shearing: Reconstruction of differential stress magnitudes and pre-deformation fluid properties. *Earth and Planetary Science Letters*, 417: 107-119.
- Doppler, G., Bakker, R.J. and Baumgartner, M., 2013. Fluid inclusion modification by H₂O and D₂O diffusion: The influence of inclusion depth, size, and shape in re-equilibration experiments. *Contributions to Mineralogy and Petrology*, 165: 1259-1274.
- Drury, M.R. and Urai, J.L., 1990. Deformation-related recrystallization processes. *Tectonophysics*, 172(3-4): 235-253.
- Dubessy, J., Poty, B. and Ramboz, C., 1989. Advances in C-O-H-N-S fluid geochemistry based on micro Raman spectrometric analysis of fluid inclusions. *European Journal of Mineralogy*, 1(4).
- Duggen, S., Hoernle, K., Van Den Bogaard, P. and Garbe-Schonberg, D., 2005. Post-Collisional Transition from Subduction- to Intraplate-type Magmatism in the Westernmost Mediterranean: Evidence for Continental-Edge Delamination of Subcontinental Lithosphere. *Journal of Petrology*, 46(6): 1155-1201.
- Duggen, S., Hoernle, K., van den Bogaard, P. and Harris, C., 2004. Magmatic evolution of the Alboran region: The role of subduction in forming the western Mediterranean and causing the Messinian Salinity Crisis. *Earth and Planetary Science Letters*, 218(1-2): 91-108.

- Dyja, V., Hibsich, C., Tarantola, A., Cathelineau, M., Boiron, M.C., Marignac, C., Bartier, D., Carrillo-Rosua, J., Morales Ruano, S. and Boulvais, P., 2016. From deep to shallow fluid reservoirs : evolution of fluid sources during the exhumation of the Sierra Almagrera (Betics, Spain). *Geofluids*, 16(1): 103-128.
- Egeler, C., 1963. On the tectonics of the eastern Betic Cordilleras (SE Spain). *Geologische Rundschau*, 53(1): 260-269.
- Egeler, C.G. and Simon, O.J., 1969. Sur la tectonique de la Zone Bétique (Cordillères Bétiques, Espagne). Etudes basées sur la recherche dans le secteur compris entre Almería y Vélez-Rubio». *Verk. Kon. Ned. Akad. V. Wetensch Afd. Nat. serts. reeks.*, 25(3): 90 p.
- Eglinger, A., Ferraina, C., Tarantola, A., André-Mayer, A. S., Vanderhaeghe, O., Boiron, M. C., Dubessy, J., Richard, A. and Brouand, M., 2014. Hypersaline fluids generated by high-grade metamorphism of evaporites: fluid inclusion study of uranium occurrences in the Western Zambian Copperbelt. *Contributions to Mineralogy and Petrology*, 167(2): 967.
- Faccenna, C., Jolivet, L., Piromallo, C., and Morelli, A., 2003. Subduction and the depth of convection in the Mediterranean mantle, *Journal of Geophysical Research*, 108(B2) DOI: 10.1029/2001JB00169.
- Famin, V. and Nakashima, S., 2004. Fluid migration in fault zones and the evolution of detachments: The example of Tinos Island (Greece). In: I. Universal Academy Press (Editor), *Physicochemistry of Water in Geological and Biological Systems*, Tokyo, Japan, pp. 189-209
- Famin, V., Philippot, P., Jolivet, L., Agard, P., 2004. Evolution of hydrothermal regime along a crustal shear zone, Tinos Island, Greece. *Tectonics*, 23: 1-23.
- Famin, V., Hébert, R., Philippot, P. and Jolivet, L., 2005. Ion probe and fluid inclusion evidence for co-seismic fluid infiltration in a crustal detachment. *Contributions to Mineralogy and Petrology*, 150(3): 354-367.

- Fircks, F. F. 1906. Über einige Erzlagerstätten der Provinz Almeria in Spanien. Zeitschrift für praktische Geologie, Jahrg. 14, 142-150: 233-236.
- Fontes, J.C. and Matray, J.M., 1993. Geochemistry and origin of formation brines from the Paris Basin, France: 1. Brines associated with Triassic salts. Chemical Geology, 109(1-4): 149-175.
- Gomez-Pugnaire, M.T. and Fernandez-Soler, J.M., 1987. High-pressure metamorphism in metabasites from the Betic Cordilleras (S.E. Spain) and its evolution during the Alpine orogeny. Contributions to Mineralogy and Petrology, 95(2): 231-244.
- Gomez-Pugnaire, M.T., Franz, G. and Sanchez-Vizcaino, V.L., 1994. Retrograde formation of NaCl-scapolite in high pressure metaevaporites from the Cordilleras Béticas (Spain). Contrib. Mineral. Petrol., 116(4): 448-461.
- Gomez-Pugnaire, M.T., Galindo-Zaldívar, J., Rubatto, D.,; Gonzalez-Lodeiro, F., Lopez Sanchez-Vizcaino, V., Jabaloy, A., 2004. A reinterpretation of the Nevado-Filabride and Alpujarride Complexes (Betic Cordillera): Field, petrography and U-Pb ages from orthogneisses (western Sierra Nevada, S Spain). Schweizerische Mineralogische und Petrographische Mitteilungen, 84(3): 303-322.
- González-Casado, J.M., Casquet, C., Martínez-Martínez, J.M. and Garcia-Dueñas, V., 1995. Retrograde evolution of quartz segregations from the Dos Picos shear zone in the Nevado-Filabride Complex (Betic chains, Spain). Evidence from fluid inclusions and quartz c-axis fabrics. International Journal of Earth Sciences, 84(1): 175-186.
- Guardiola, R. and Sierra, A., 1925. Criaderos de hierro de España: Hierros de Almería y Granada, Instituto Geológico y Minero de España : Volume 5.
- Gunther, D. and Heinrich, C.A., 1999. Enhanced sensitivity in laser ablation-ICP mass spectrometry using helium-argon mixtures as aerosol carrier. Journal of Analytical Atomic Spectrometry, 14(9): 1363-1368.

- Hirth, G. and Tullis, J., 1992. Dislocation creep regimes in quartz aggregates. *J. Struct. Geol.*, 14: 145-159.
- Ingebritsen, S.E. and Manning, C.E., 2002. Diffuse fluid flux through orogenic belts: Implications for the world ocean. *Proceedings of the National Academy of Sciences USA*, 99: 9,113-9,116.
- Jabaloy, A., Galindo-Zaldívar, J. and González-Lodeiro, F., 1993. The Alpujarride-Nevaldo-Fibábride extensional shear zone, Betic Cordillera, SE Spain. *Journal of Structural Geology*, 15(3-5): 555-569.
- Johnson, C., Harbury, N. and Hurford, A.J., 1997. The role of extension in the Miocene denudation of the Nevado-Filábride Complex, Betic Cordillera (SE Spain). *Tectonics*, 16(2): 189-204.
- Johnson, E.L. and Hollister, L.S., 1995. Syndeformational fluid trapping in quartz: determining the pressure- temperature conditions of deformation from fluid inclusions and the formation of pure CO₂ fluid inclusions during grain-boundary migration. *Journal of Metamorphic Geology*, 13(2): 239-249.
- Jolivet, L., Faccenna, C., Goffé, B., Burov, E. and Agard, P., 2003. Subduction tectonics and exhumation of high-pressure metamorphic rocks in the Mediterranean orogens. *American Journal of Science*, 303: 353-409.
- Jolivet, L., Augier, R., Faccenna, C., Negro, F., Rimmelé, G., Agard, P., Robin, C., Rossetti, F and Crespo-Blanc, A., 2008. Subduction, convergence and the mode of backarc extension in the Mediterranean region. *Bulletin de la Société Géologique de France*, 179(6): 525-550.
- Kerrich, R., 1976. Some effects of tectonic recrystallisation on fluid inclusions in vein quartz. *Contributions to Mineralogy and Petrology*, 59(2): 195-202.
- Kerrich, R., 1986. Fluid transport in lineaments. *Royal Society of London Philosophical Transactions*, ser. A, 317: 219-251.

- Kerrick, R., La Tour, T.E. and Willmore, L., 1984. Fluid participation in deep fault zones: Evidence from geological, geochemical, and $18\text{O}/16\text{O}$ relations. *Journal of Geophysical Research* 89: 4331-4343.
- Kohlstedt, D.L., Evans, B. and Mackwell, S.J., 1995. Strength of the lithosphere: constraints imposed by laboratory experiments. *Journal of Geophysical Research*, 100: 17587-17602.
- Leisen, M., 2011. Analyse chimique des inclusions fluides par ablation-laser couplée à l'ICPMS et applications géochimiques. Université de Lorraine, Nancy, France, 318 pp.
- Leisen, M., Dubessy, J., Boiron, M.-C. and Lach, P., 2012a. Improvement of the determination of element concentrations in quartz-hosted fluid inclusions by LA-ICPMS and Pitzer thermodynamic modeling of ice melting temperature. *Geochimica et Cosmochimica Acta*, 90(0): 110-125.
- Leisen, M., Boiron, M.-C., Richard, A. and Dubessy, J., 2012b. Determination of Cl and Br concentrations in individual fluid inclusions by combining microthermometry and LA-ICPMS analysis: Implications for the origin of salinity in crustal fluids. *Chemical Geology*, 330-331(0): 197-206.
- Lespinasse, M., Desindes, L., Fratzak, P. and Petrov, V., 2005. Microfissural mapping of natural cracks in rocks: Implications for fluid transfers quantification in the crust. *Chemical Geology*, 223(1-3): 170-178.
- Lister, G.S., Etheridge, M.A. and Symonds, P.A., 1986. Detachment faulting and the evolution of passive continental margins. *Geology* 14: 246-250.
- Longerich, H.P., Jackson, S.E. and Gunther, D., 1996. Inter-laboratory note. Laser ablation inductively coupled plasma mass spectrometric transient signal data acquisition and analyte concentration calculation. *Journal of Analytical Atomic Spectrometry*, 11(9): 899-904.
- Lopez Ruiz, J. and Rodriguez Badiola, E., 1980. La region volcanica neogena del sureste de Espana. *Estudios Geologicos*, 36(1-2): 5-63.

- Loreto, M.F., Tinivella, U. and Ranero, C.R., 2007. Evidence for fluid circulation, overpressure and tectonic style along the Southern Chilean margin. *Tectonophysics* 429: 183-200.
- Lupker, M., France-Lanord, C., Galy, V., Lavé, J., Gaillardet, J., Prasad Gajurel, A., Guilmette, C., Rahman, M., Kumar Singh, S. and Sinha, R., 2012. Predominant floodplain over mountain weathering of Himalayan sediments (Ganga basin). *Geochimica et Cosmochimica Acta*, 84: 410-432.
- Manning, C.E. and Ingebritsen, S.E., 1999. Permeability of the continental crust: The implications of geothermal data and metamorphic systems. *Reviews of Geophysics*, 37: 127-150.
- Martínez-Martínez, J.M., 1986. Evolución tectono-metamórfica del Complejo Nevado-Filábride en el sector de unión entre Sierra Nevada y Sierra de los Filabres (Cordilleras Béticas, España). *Cuadernos de Geología de la Universidad de Granada (edición especial)*, 13: 194 pp.
- Martínez-Martínez, J.M. and Azañón, J.M., 2002. Orthogonal extension in the hinterland of the Gibraltar Arc (Betics, SE Spain), in *Reconstruction of the evolution of the Alpine-Himalayan Orogen*. *Journal of the Virtual Explorer*, 8: 3-22.
- Martínez-Martínez, J.M., Soto, J.I. and Balanya, J.C., 2002. Orthogonal folding of extensional detachments: Structure and origin of the Sierra Nevada elongated dome (Betics, SE Spain). *Tectonics*, 21(3): 1-20.
- Martínez-Martínez, J.M., Torres-Ruiz, J., Pesquera, A. and Gil-Crespo, P.P., 2010. Geological relationships and U-Pb zircon and $^{40}\text{Ar}/^{39}\text{Ar}$ tourmaline geochronology of gneisses and tourmalinites from the Nevado-Filabride complex (western Sierra Nevada, Spain): Tectonic implications. *Lithos*, 119(3-4): 238-250.
- McCaig, A.M., 1988. Deep fluid circulation in fault zones. *Geology*, 16: 867-870.
- Menzies, C.D., Teagle, D.A. H., Craw, D., Cox, S.C., Boyce, A.J., Barrie, C.D. and Roberts, S., 2014. Incursion of meteoric waters into the ductile regime in an active orogen. *Earth and Planetary Science Letters*, 399: 1-13.

- Menzies, C.D., Teagle, D.A.H., Niedermann, S., Cox, S.C, Craw, D., Zimmer, M., Cooper, M.J. and Erzinger, J., 2016. The fluid budget of a continental plate boundary fault: Quantification from the Alpine Fault, New Zealand. *Earth and Planetary Science Letters*, 445: 125-135.
- Mezri, L., Le Pourhiet, L., Wolf, S. and Burov, E., 2015. New parametric implementation of metamorphic reactions limited by water content, impact on exhumation along detachment faults. *Lithos*, 236-237: 287-298
- Miller, E.L, Gans, P.B. and Garing, J., 1983. The Snake Range Decollement: An exhumed mid-Tertiary ductile-brittle transition. *Tectonics*, 2: 239-263.
- Montenat, C. and Ott d'Estevou, P., 1990. Eastern Betic Neogene basins-a review. D.E.T.I.s (Ed.) : Les bassins néogènes de domaines bétique oriental (Espagne), 12-13: 9-15.
- Montenat, C. and Ott d'Estevou, P., 1999. The diversity of late Neogene sedimentary basins generated by wrench faulting in the eastern Betic cordillera, SE Spain. *Journal of Petroleum Geology*, 22(1): 61-80.
- Morrison, J., 1994. Meteoric water-rock interaction in the lower plate of the Whipple Mountain metamorphic core complex, California. *Journal of metamorphic Geology*, 12(6): 827-840.
- Nijhuis, H.J., 1964, Plurifacial alpine metamorphism in the south-eastern Sierra de los Filabres south of Lubrín, SE Spain, Aka-demisch proefschrift, Universiteit van Amsterdam, 151 pp.
- Oliver, N.H.S., 1996. Review and classification of structural controls on fluid flow during regional metamorphism. *Journal of Metamorphic Geology*, 14(4): 477-492.
- Passchier, C.W. and Trouw, R.A.J., 2005. *Microtectonics*. Springer, Berlin, 366 pp.
- Pearce, N.J.G., Perkins, W.T., Westgate, J.A., Gorton, M.P., Jackson, S.E., Neal, C.R. and Chenery, S.P., 1997. A Compilation of New and Published Major and Trace Element Data for NIST SRM 610 and NIST SRM 612 Glass Reference Materials. *Geostandards Newsletter*, 21(1): 115-144.

- Pérez-López, A., Pérez-Valera, F. and Götz, A. E., 2012. Record of epicontinental platform evolution and volcanic activity during a major rifting phase: The Late Triassic Zamoranos Formation (Betic Cordillera, S Spain). *Sedimentary Geology*, 247: 39-57.
- Platt, J.P., 2007. From orogenic hinterlands to Mediterranean-style back-arc basins: a comparative analysis. *Journal of the Geological Society*, 164(2): 297-311.
- Platt, J.P., Anczkiewicz, R., Soto, J.I., Kelley, S.P. and Thirlwall, M., 2006. Early Miocene continental subduction and rapid exhumation in the western Mediterranean. *Geology*, 34(11): 981-984.
- Prelevic, D., Foley, S.F., Romer, R. and Conticelli, S., 2008. Mediterranean Tertiary lamproites derived from multiple source components in postcollisional geodynamics. *Geochimica et Cosmochimica Acta*, 72(8): 2125-2156.
- Puga, E., Nieto, J.M. and De Federico, A.D., 2000. Contrasting P-T paths in eclogites of the betic ophiolitic association, Mulhacen Complex, Southeastern Spain. *The Canadian Mineralogist*, 38(5): 1137-1161.
- Reynolds, S.J. and Lister, G.S., 1987. Structural aspects of fluid-rock interactions in detachment zones. *Geology*, 15: 362-366.
- Richard, A., Cathelineau, M., Boiron, M. C., Mercadier, J., Banks, D. A. and Cuney, M. (2016). Metal-rich fluid inclusions provide new insights into unconformity-related U deposits (Athabasca Basin and Basement, Canada). *Mineralium Deposita*, 51(2) : 249-270.
- Sanz de Galdeano, C. and Garcia Tortosa, F.J., 2002. Alpujarride attribution of the supposed 'Almagrider Complex' (Betic Internal Zone, Almeria Province, Spain). *Comptes Rendus Geoscience*, 334(5): 355-362.
- Scheffer, C., Tarantola, A., Vanderhaeghe, O., Rigaudier, T. and Photiades, A., 2017. CO₂ flow during orogenic gravitational collapse: Syntectonic decarbonation and fluid mixing at the ductile-brittle transition (Lavrion, Greece). *Chemical Geology* 450: 248-263.

- Scheffer, C., Tarantola, A., Vanderhaeghe, O., Voudouris, P., Rigaudier, T., Photiades, A., Morin, D. and Alloucherie, A. (2017) The Lavrion Pb-Zn-Fe-Cu-Ag detachment-related district (Attica, Greece): Structural control on hydrothermal flow and element transfer-deposition. *Tectonophysics* 717: 607-627.
- Serrano, F., Sanz de Galdeano, C., El Kadiri, K., Guerra-Merchán, A., López-Garrido, A.C., Martin-Martin, M. and Hlila, R., 2006. Oligocene-early Miocene transgressive cover of the Betic-Rif Internal Zone. Revision of its geologic significance. *Eclogae Geologicae Helvetiae*, 99(2): 237-253.
- Sheppard, S., 1986. Characterization and isotopic variations in natural waters. *Reviews in Mineralogy*, 16: 165-183.
- Siebenaller, L., Boiron, M.C., Vanderhaeghe, O., Hibsich, C., Jessell, M.W., André-Mayer, A.S., France-Lanord, C. and Photiades, A., 2013. Fluid record of rock exhumation across the brittle–ductile transition during formation of a Metamorphic Core Complex (Naxos Island, Cyclades, Greece). *Journal of Metamorphic Geology*, 31(3): 313-338.
- Siebenaller, L., Vanderhaeghe O., Jessell M., Boiron M.C. and Hibsich C., 2016. Syntectonic fluids redistribution and circulation coupled to quartz recrystallization in the ductile crust (Naxos Island, Cyclades, Greece). *Journal of Geodynamics*, 101: 129-141.
- Smith, M.P., Gleeson, S.A. and Yardley, B.W.D., 2013. Hydrothermal fluid evolution and metal transport in the Kiruna District, Sweden: Contrasting metal behaviour in aqueous and aqueous-carbonic brines. *Geochimica et Cosmochimica Acta*, 102(0): 89-112.
- Soto, J.I., García-Dueñas, V. and Martínez-Martínez, J.M., 1990. Valor de la deformación dúctil asimétrica en el Ortogneis de Lubrín (Manto de Bédar-Macael, Complejo Nevado-Filábride, Béticas). *Geogaceta*, 7: 92-94.
- Steele-MacInnis, M., Bodnar, R.J. and Naden, J., 2011. Numerical model to determine the composition of H₂O-NaCl-CaCl₂ fluid inclusions based on microthermometric and microanalytical data. *Geochimica Cosmochimica Acta*, 75: 21-40.

- Sterner, S.M. and Bodnar, R.J., 1989. Synthetic fluid inclusions. VII. Reequilibration of fluid inclusions in quartz during laboratory-simulated metamorphic burial and uplift. *Journal of Metamorphic Geology*, 7: 243-260.
- Stipp, M., Stünitz, H., Heilbronner, R. and Schmid, S.M., 2002. The eastern Tonale fault zone: a "natural laboratory" for crystal plastic deformation of quartz over a temperature range from 250 to 700 °C. *Journal of Structural Geology*, 24(12): 1861-1884.
- Stünitz, H., Thust, A., Heilbronner, R., Behrens, H., Kilian, R., Tarantola A. and Fitz Gerald, J.D., 2017. Water redistribution in experimentally deformed natural milky quartz single crystals- Implications for H₂O-weakening processes. *J. Geophys. Res. Solid Earth* 122, doi:10.1002/2016JB013533.
- Suzuoki, T. and Epstein, S., 1976. Hydrogen isotope fractionation between OH-bearing minerals and water. *Geochimica and Cosmochimica Acta*, 40: 1229-33.
- Tarantola, A., Diamond, L. and Stünitz, H., 2010. Modification of fluid inclusions in quartz by deviatoric stress I: experimentally induced changes in inclusion shapes and microstructures. *Contributions to Mineralogy and Petrology*, 160: 825-843.
- Tarantola, A., Diamond, L.W., Stünitz, H., Thust, A. and Pec, M., 2012. Modification of fluid inclusions in quartz by deviatoric stress III: Influence of principal stresses on inclusion density and orientation. *Contributions to Mineralogy and Petrology*, 164 (3): 537-550.
- Tobisch, O.T., Barton, M.D., Vernon, R.H., Paterson, S.R., 1991. Fluid-enhanced deformation: Transformation of granitoids to banded mylonites, western Sierra Nevada, California, and southeastern Australia. *J. Struct. Geol.*, 13: 1137-1156.
- Torres-Ruiz, J., 1983. Genesis and evolution of the Marquesado and adjacent iron ore deposits, Granada, Spain. *Econ. Geol.*, 78(8): 1657-1673.
- Torres-Ruiz, J., 2006. Geochemical constraints on the genesis of the Marquesado iron ore deposits, Betic Cordillera, Spain: REE, C, O, and Sr isotope data. *Econ. Geol.*, 101(3): 667-677.

- Tullis, J. and Yund, R.A., 1987. Transition from cataclastic flow to dislocation creep of feldspar : mechanisms and microstructures. *Geology*, 15: 606-609.
- Upton, P., Koons, P.O. and Chamberlain, C.P., 1995. Penetration of deformation-driven meteoric water into ductile rocks: isotopic and model observations from the Southern Alps, New Zealand. *New Zealand Journal of Geology and Geophysics*, 38: 535-543.
- Urai, J.L., Means, W.D. and Lister, G.S., 1986. Dynamic recrystallization of minerals. *Am. Geoph. Union, Geoph. Monogr.*
- Van Den Kerkhof, A.M. and Hein, U.F., 2001. Fluid inclusion petrography. *Lithos*, 55(1-4): 27-47.
- Vanko, D.A., Bodnar, R.J. and Sterner, S.M., 1988. Synthetic fluid inclusions: VIII. Vapor-saturated halite solubility in part of the system NaCl-CaCl₂-H₂O, with application to fluid inclusions from oceanic hydrothermal systems. *Geochimica et Cosmochimica Acta*, 52(10): 2451-2456.
- Vapnik, Y. and Avigad, D., 2004. P-T conditions of quartz-calcite boudins and vein formation within a low-angle detachment fault in Tinos Island (Aegean Sea): a fluid-inclusion study. *International Journal of Earth Sciences*, 93(4): 487-499.
- Vera, J.A., 2001. Evolution of the South Iberian Continental Margin. *Mémoires du Muséum national d'histoire naturelle* 186 109-143.
- Wernicke, B., 1981. Low-angle normal faults in the Basin and Range Province: nappe tectonics in an extending orogen. *Nature* 191: 645-648.
- Westra, G., 1969. Petrogenesis of a composite metamorphic facies series in an intricate fault zone of the southeastern Sierra Cabrera (SE, Spain), Free University, Amsterdam, Amsterdam, 166 pp.
- Wickham, S.M., Peters, M.T., Fricke, H.C. and O'Neil, J.R., 1993. Identification of magmatic and meteoric fluid sources and upward- and downward-moving infiltration fronts in a metamorphic core complex. *Geology* 21, 81-84.

- Wilkins, R.W.T. and Barkas, J.P., 1978. Fluid inclusions, deformation and recrystallization in granite tectonites. *Contributions to Mineralogy and Petrology*, 65(3): 293-299.
- Wilkinson, J.J., Jenkin, G.R.T., Fallick, A.E. and Foster, R.P., 1995. Oxygen and hydrogen isotopic evolution of Variscan crustal fluids, south Cornwall, U.K. *Chemical Geology*, 123(1&4): 239-254.
- Yardley, B. W., 2005. 100th Anniversary Special Paper: metal concentrations in crustal fluids and their relationship to ore formation. *Economic Geology*, 100(4), 613-632.
- Yardley, B.W.D. and Graham, J.T., 2002. The origins of salinity in metamorphic fluids. *Geofluids*, 2(4): 249-256.
- Zeck, H.P., Albat, F., Hansen, B.T., Torres-Roldán, R.L. and García-Casco, A., 1989. Alpine tourmaline-bearing muscovite leucogranites, intrusion age and petrogenesis, Betic Cordilleras, SE Spain. . *Neues Jahrbuch für Mineralogie, Monatshefte*: 513-520.
- Zeck, H.P., Kristensen, A.B. and Nakamura, E., 1999. Inherited Palaeozoic and Mesozoic Rb-Sr isotopic signatures in Neogene calc-alkaline volcanics, Alborán Volcanic Province, SE Spain. *Journal of Petrology*, 40(4): 511-524.
- Zhang, Y.-G. and Frantz, J.D., 1987. Determination of the homogenization temperatures and densities of supercritical fluids in the system NaCl-KCl-CaCl₂-H₂O using synthetic fluid inclusions. *Chemical Geology*, 64(3-4): 335-350.
- Zheng, Y.-F., 1993. Calculation of oxygen isotope fractionation in anhydrous silicate minerals. *Geochimica et Cosmochimica Acta*, 57(5): 1079-1091.

Table captions

Table 1: Nomenclature, definitions and abbreviations of terms describing the veins.

Table 2: Abbreviations for phases and temperatures of phase transitions observed during microthermometric experiments on fluid inclusions.

Table 3: Whole rock analyses of unaltered and bleached orthogneiss at a few centimetres from V-dis veins. LOI: loss on ignition.

Table 4: Microthermometric and compositional data for fluid inclusions from V-par and V-dis veins. All fluid inclusions are water-dominated and homogenize into liquid by disappearance of the CO₂ gas phase. Data are presented as min./max. values. Values in italics indicate mode and number of analyses, respectively.

Table 5: Fluid inclusion halogen compositions in V-par and V-dis veins. n.a.: not analysed. [Cl]: mean Cl concentration of fluid inclusions in the bulk sample derived from the salinity data determined from microthermometry. Cl/Br ratios determined by bulk crush-leach analysis are quoted with an uncertainty of 5 %. Cl/Br ratios determined by LA-ICP-MS on individual fluid inclusions are quoted with an uncertainty of 30 %.

Table 6: LA-ICP-MS data showing major and minor elements concentrations in individual fluid inclusions from two sets of V-par and V-dis veins from the Sierra Bédar. Typical uncertainties range from 10 to 30 % for Na, Ca, K and Mg and from 30 to 50 % for Li, Fe and Sr). Values preceded by a < symbol stand for element concentrations below the limit of detection.

Table 7: Isotopic compositions of host-rock quartz and micas, vein quartz, and fluid inclusions, with calculated isotopic composition of the fluid and the apparent equilibrium temperatures between white micas and quartz-hosted fluid inclusions. White micas are from the orthogneiss outside the bleached area at the contact with the vein. The last four lines correspond to δD analyses of schist layers intercalated within the gneiss. All $\delta^{18}O$ and δD values are expressed in ‰ (V-SMOW). Sites are located in Fig. 2. n.a.: not analysed. ⁽¹⁾ Calculated using equation of Zheng (1993) for quartz-H₂O fractionation at 400 °C based on reconstruction of fluid inclusion *PT* conditions (see discussion). ⁽²⁾ Calculated using equation of Suzuoki and Epstein (1976) for muscovite-H₂O fractionation.

ACCEPTED MANUSCRIPT

Figure captions

Figure 1: Location of the study area. (a) Geological context of the Eastern Betics and location of the Sierra Bédar (modified after Augier (2004)). The main lithological units and structures (including the Mecina-Filabres detachment) are indicated. (b) Map showing the directions of the stretching lineation and sense of ductile shear in the hanging-wall and the trajectories defining the directions of maximum stretching (Johnson et al., 1997; Jabaloy et al., 1993) (c) Simplified map showing orthogneissic layers and the main metamorphic units (modified after Soto et al. (1990)). (d) Stereodiagrams showing the poles of V-dis quartz veins rotated back to horizontal foliation position. Sampling sites are indicated in (c). (e) NW-SE cross-section located on (c).

Figure 2: Field relationships between V-dis veins and V-par veins and host-rocks. (a) and (b) show a decimetre-scale corrugation feature with two directions of exposure (5 € cents as scale for both photos). The extension and related vein opening direction is parallel to the fold axis and stretching lineation (indicated by red arrows). The close-up shows the connection between the quartz from V-dis veins and V-par veins is shown in the inset. (c) represents the 3D interpretation of the relationship between vein opening and host rock deformation in a bloc diagram. Mineral lineation due to ductile shearing is parallel to the corrugation axis. (d) brittle V-dis affect orthogneissic layers while micaschist layers acted as ductile relay zones. (e) micaschist layer is also affected by V-dis vein when associated with normal displacement as indicated by white arrow.

Figure 3: Petrography of V-par and V-dis veins. (a) V-par foliation-parallel quartz-tourmaline veins. (b) V-par milky quartz veins and V-dis quartz vein associated with normal faulting. (c) N-S striking V-dis (with heterogeneous bleaching alteration halo) discordant to the foliation. (d) to (i) Microphotographs of quartz microstructures and fluid inclusion distribution (cross-polarised

light - CPL). Some colour variations within the same quartz grain may be due to the photomontage. Both quartz grains in V-par (e) and V-dis (d) display undulatory extinction. Qrem: remnant quartz, Qrxt(1) and Qrxt(2) : recrystallized quartz, FIP : Fluid Inclusions Planes, Qz: quartz, Fsp: Feldspar.

Figure 4: Microphotographs showing the petrography of fluid inclusions. (a) Examples of intragranular fluid inclusion planes in quartz grains from V-par and V-dis. (b) Example of H₂O-salt-CO₂-N₂ slightly irregular fluid inclusion in V-par. (c) Example of H₂O-salt-CO₂-N₂ fluid inclusion in V-dis. Stereodiagrams showing the poles of direction and dip of fluid inclusion planes in V-par and V-dis are displayed in (b) and (c) respectively. (d) Example of H₂O-salt-CO₂-N₂-carbonate fluid inclusion that can be found either in V-par and V-dis.

Figure 5: Diagram showing homogenization temperature ($T_h(L)$ (°C)) vs. salinity (mass.% NaCl + CaCl₂) of fluid inclusions from V-par and V-dis veins. Deformed and undeformed (normal) inclusions are distinguished.

Figure 6: Vapour saturated phase equilibria in the ternary H₂O-NaCl-CaCl₂ system. Isotherms of halite dissolution and ice melting are shown with temperatures given in degrees Celsius (modified after Vanko et al., 1988). Fluid inclusion compositions are determined using $T_m(hl)$ - $T_m(ice)$ pairs according to Steele-MacInnis et al. (2011). HH : Hydrohalite.

Figure 7: Cl/Br molar ratio vs. Cl concentrations for fluid inclusions analysed by LA-ICP-MS and crush-leach methods obtained on the various V-par and V-dis veins. The seawater evaporation trend is indicated (Fontes and Matray, 1993): SW: Seawater, G: Gypsum, H: Halite, E: Epsomite, S: Sylvite, C: Carnallite, B: Bischofite. Field A—Halite-dissolution brines associated

with emerald mineralization in Columbia (Banks et al., 2000) and B—Magmatic brines (35-40 mass% NaCl eq.) (Böhlke and Irwin, 1992; Smith et al., 2013).

Figure 8: Diagram showing distribution of various element concentrations (in ppm) in fluid inclusions from V-par and V-dis veins (grey and red respectively), as determined by LA-ICP-MS analysis. Each line corresponds to one fluid inclusion analysis.

Figure 9: Reconstructed $\delta^{18}\text{O}_{\text{fluid}} \text{‰ V-SMOW}$ vs. $\delta\text{D}_{\text{fluid}} \text{‰ V-SMOW}$ values for V-par and V-dis fluid inclusions. Fields of some representative fluids from the literature: basinal fluids (GC = Gulf Coast; C = California; M= Michigan), metamorphic and magmatic fluids are after Sheppard (1986). The grey domains represent the expected $\delta\text{D}_{\text{fluid}}$ values considering equilibrium with the white micas of the host-rock. Isotopic equilibrium calculation are made at 400 and 600 °C using the whole range of $\delta\text{D}_{\text{white micas}}$ values for orthogneiss and intercalated schists given in Table 7 (i.e. -35.4 to $-45.6 \pm 2 \text{‰}$ and -99.3 to $-101.5 \pm 2 \text{‰}$, respectively) with the equation of Suzuoki and Epstein (1976) for muscovite- H_2O fractionation. Most isotopic values of water from fluid inclusions show equilibration with white micas of the orthogneiss.

Figure 10: *PT* trapping conditions of fluid inclusions. (a) and (b) isochores for fluid inclusions from V-par and V-dis veins respectively. (c) and (d) *PT* trapping conditions of fluid inclusions from V-par and V-dis veins respectively after: (i) isochoric reconstructions shown in (a) and (b); (ii) quartz deformation features and (iii) and literature data on *PT* evolution of the the Bédar-Macael units (De Jong, 1992; Augier et al., 2005a). The ages are from Augier et al. (2005a).

Abbreviations: Qtz: quartz; Fld: Feldspar; g.g.l.p.: geothermal gradient at lithostatic pressure.

Brittle/Ductile transitions of quartz, feldspar and micas from Passchier and Trouw (2005).

Figure 11: Source of fluids in the Nevado-Filabride complex trapped in quartz veins affecting a brittle orthogneissic body below the active detachment system. The brines trapped in the quartz veins originate from dissolution of Triassic metaevaporites by metamorphic fluids variably enriched in Br by interaction with graphitic schists. Local brittle conditions in the orthogneiss within a unit of ductile lithologies were not sufficient to allow surficial fluids to penetrate the detachment footwall. The crustal-scale DBT (ductile-brittle transition zone) played the role of hydrogeological barrier preventing surficial fluids penetration. B.M.: Bedar Macael unit, B.C.: Ballabona-Cucharón unit, C.A.: Calar Alto unit.

ACCEPTED MANUSCRIPT

Table 1

Vein type	Vein / rock foliation relationships	Vein mineralogy
V-par	Parallel to the rock foliation	Quartz (translucent or milky) - tourmaline - micas
V-dis	Discordant to the rock foliation	Quartz

ACCEPTED MANUSCRIPT

Table 2

Abbreviation	Observation
L	Liquid
V	Vapour
S	Solid
Flw	Volumetric fraction of the aqueous liquid at room temperature
T_e	Apparent eutectic temperature (i.e. first melting)
$T_m(\text{ice})$	Final melting temperature of ice
$T_m(\text{hl})$	Dissolution temperature of halite
$T_h(\text{L})$	Bulk homogenization temperature to the liquid phase ($L+V=L$)

ACCEPTED MANUSCRIPT

Table 3

Oxides (wt.%)	SiO ₂	Al ₂ O ₃	Fe ₂ O ₃	MnO	MgO	CaO	Na ₂ O	K ₂ O	TiO ₂	P ₂ O ₅	LOI	Total
Bleached orthogneiss (around V-dis)	78.54	13.04	0.38	0	0.04	0.48	7.61	0.11	0.09	0.22	0.42	100.93
Orthogneiss	77.15	13.11	1.21	0.01	0.16	0.37	3.77	3.9	0.11	0.23	0.87	100.87

Elements (ppm)	As	Ba	Be	Bi	Cd	Ce	Co	Cr	Cs	Cu	Dy	Er	Eu	Ga
Bleached orthogneiss (around V-dis)	20.24	8.87	0.83	1.97	0.26	9.7	14.42	<lod	0.39	15.04	1.8	0.55	0.16	18.6
Orthogneiss	31.2	52.55	1.03	2.76	<lod	14.73	1.23	<lod	30.24	<lod	2.15	0.64	0.17	21.07

Elements (ppm)	Gd	Ge	Hf	Ho	In	La	Lu	Mo	Nb	Nd	Ni	Pb	Pr	Rb	Sc
Bleached orthogneiss (around V-dis)	1.93	2.19	2.54	0.27	<lod	4.27	0.06	<lod	9.04	5.72	7.2	9.48	1.44	6.33	<lod
Orthogneiss	2.34	2.53	2.28	0.32	0.21	5.89	0.07	<lod	9.11	7.35	<lod	10.33	1.9	441.8	3.53

Elements (ppm)	Sb	Sm	Sn	Sr	Ta	Tb	Th	Tm	U	V	W	Y	Yb	Zn	Zr
Bleached orthogneiss (around V-dis)	1.23	1.89	6.94	65.87	2.27	0.34	5.05	0.07	1.17	3.59	2.8	7.89	0.4	16.82	61
Orthogneiss	0.48	2.42	28.36	36.2	2.42	0.42	8.31	0.08	1.24	4.62	10.39	9.36	0.47	38.3	54.04

Table 4

Vein type	Microthermometry				Gas composition		
	T_e (°C)	$T_m(\text{ice})$ (°C)	$T_m(\text{hl})$ (°C)	T_h (°C)	Salinity (mass% NaCl + CaCl ₂)	CO ₂ (mole %)	N ₂ (mole %)
V-par	-75/-40	-38/-18	130/240	210/365	29.7/37.6	60/100	0/40
	-60	-28	183	330	34	80	19
	35	46	28	41	26	27	27
V-dis	-70/-35	-43/-19	160/280	220/400	30.8/41.3	80/100	0/20
	-59	-30	222	281	37	92	8
	34	38	31	36	27	25	25

Table 5

Sample N°	Site (Fig. 1d)	Vein type	[Cl] (mmol/kg)	Cl/Br (molar) Crush-leach	Cl/Br (molar) LA-ICP-MS
VD-12.4.9-11	1	V-par	5700	990	310-2400
VD-20.10.10-3	1	V-par	5000	295	n.a.
VD-5.4.9-7	1	V-dis	5900	170	n.a.
VD-12.4.9-4A	SE Bédar	V-dis	4700	320	n.a.
VD-12.4.9-7	2	V-dis	5900	1440	730-4500
VD-12.4.9-9	1	V-dis	5300	500	210-1700
VD-12.4.9-10	1	V-dis	5500	600	250-2400
VD-20.10.10-1	1	V-dis	6100	1475	n.a.
VD-21.10.10-1	3	V-dis	4900	1275	n.a.
VD-21.10.10-3	3	V-dis	5700	630	n.a.

Table 6

(ppm)	Na	Li	Mg	K	Ca	Fe	Cu	Zn	Sr	Ba	Pb
V-par	59000	690	11000	14000	22000	2800	<130	<120	1200	<145	<120
	70000	1000	9400	25000	-	6000	<230	<160	980	<110	<140
	58000	770	4100	30000	23000	4600	1200	720	1000	300	<100
	50000	1300	8300	18000	24000	8500	<260	<180	2600	1200	530
	80000	980	6500	21000	-	5600	500	420	880	880	160
	54000	800	19000	17000	8100	5300	<110	<60	1000	570	<180
	59000	1200	13000	22000	10000	6100	<50	380	1000	540	200
	60000	640	14000	19000	10000	5000	<140	<120	1300	1200	<120
	60000	1100	4100	31000	17000	8500	<70	430	1800	2000	140
	48000	1600	4600	45000	18000	8800	<240	700	1900	1300	240
	55000	1700	8300	29000	13000	10000	<80	840	1200	240	150
	41000	1300	7700	42000	24000	6300	<90	650	1300	<150	250
	69000	650	4800	20000	18000	5700	<150	410	760	470	380
	49000	580	14000	18000	20000	5700	<90	800	650	<100	<100
	66000	1100	1600	35000	18000	5600	<140	420	1300	870	190
V-dis	71000	<70	4900	27000	15000	5000	<120	960	630	<150	530
	69000	<100	3500	16000	16000	15000	<140	770	660	<120	350
	75000	<60	11000	21000	15000	4700	<90	710	640	3400	430
	81000	<80	8100	21000	15000	5000	220	820	630	<130	460
	75000	<110	8100	29000	12000	8100	<50	1090	660	<90	420
	74000	<100	6100	22000	10000	7300	<130	880	650	<150	350

Table 7

Sample N°	Site (Fig. 1d)	Type of sample	$\delta^{18}\text{O}_{\text{quartz}}$ vein	$\delta^{18}\text{O}_{\text{quartz}}$ host-rock	$\delta^{18}\text{O}_{\text{fluid}}^{(1)}$	$\delta\text{D}_{\text{fluid}}$	$\delta\text{D}_{\text{white micas}}$	$T_{\text{equilibrium}}^{(2)}$ (°C)
VD-5.4.9-6	1	V-par	13.6 ±0.5	18.7 ±0.5	7.2 - 11.5	-39.8 ±3	-42.7 ±2	729
VD-12.4.9-11	1	V-par	13.8 ±0.5	n.a.	7.4 - 11.7	-27.8 ±3	n.a.	n.a.
VD-20.10.10-3	1	V-par	12.6 ±0.5	17.8 ±0.5	6.2 - 10.5	-29.9 ±3	-40.2 ±2	593
VD-5.4.9-7	1	V-dis	14.2 ±0.5	18.7 ±0.5	5.2 - 9.7	-24.8 ±3	-42.7 ±2	499
VD-12.4.9-4A	SE Bédar	V-dis	15.4 ±0.5	18.3 ±0.5	6.4 - 10.9	-29.8 ±3	-43.9 ±2	542
VD-12.4.9-4B	SE Bédar	V-dis	13.4 ±0.5	18.3 ±0.5	4.4 - 8.9	-28.5 ±3	-43.9 ±2	527
VD-12.4.9-7	2	V-dis	14.1 ±0.5	n.a.	5.1 - 9.6	-23.6 ±3	-35.4 ±2	572
VD-12.4.9-9	1	V-dis	14.3 ±0.5	n.a.	5.3 - 9.8	-16.7 ±3	-35.4 ±2	491
VD-12.4.9-10	1	V-dis	13.4 ±0.5	n.a.	4.4 - 8.9	-26.4 ±3	n.a.	
VD-20.10.10-1	1	V-dis	13.9 ±0.5	17.8 ±0.5	4.9 - 9.4	-25.3 ±3	-40.2 ±2	532
VD-21.10.10-1	3	V-dis	13.9 ±0.5	18.2 ±0.5	4.9 - 9.4	-22.3 ±3	-45.6 ±2	448
VD-21.10.10-3	3	V-dis	14.3 ±0.5	18.2 ±0.5	5.3 - 9.8	-32.8 ±3	-38.1 ±2	678
CHBe-14-10	1	Schist				[-39.8 / -16.7]	-101.5 ±2	[188 / 249]
CHBe-14-11	1	Schist				[-39.8 / -16.7]	-99.3 ±2	[192 / 257]
CHBe-14-7a	1	Schist				[-39.8 / -16.7]	-99.8 ±2	[191 / 255]
CHBe-14-7b	1	Schist				[-39.8 / -16.7]	-96.9 ±2	[198 / 265]

Dyja-Person et al. Highlights

Fluid inclusions in the detachment foot-wall of a metamorphic core complex are targeted.

Multi-analytical approach are used to characterize the fluid inclusions.

Only metamorphic brines are recorded.

The brines acquired their high salinity through dissolution of Triassic evaporites.

No infiltration of surficial fluids is recorded during exhumation.

ACCEPTED MANUSCRIPT

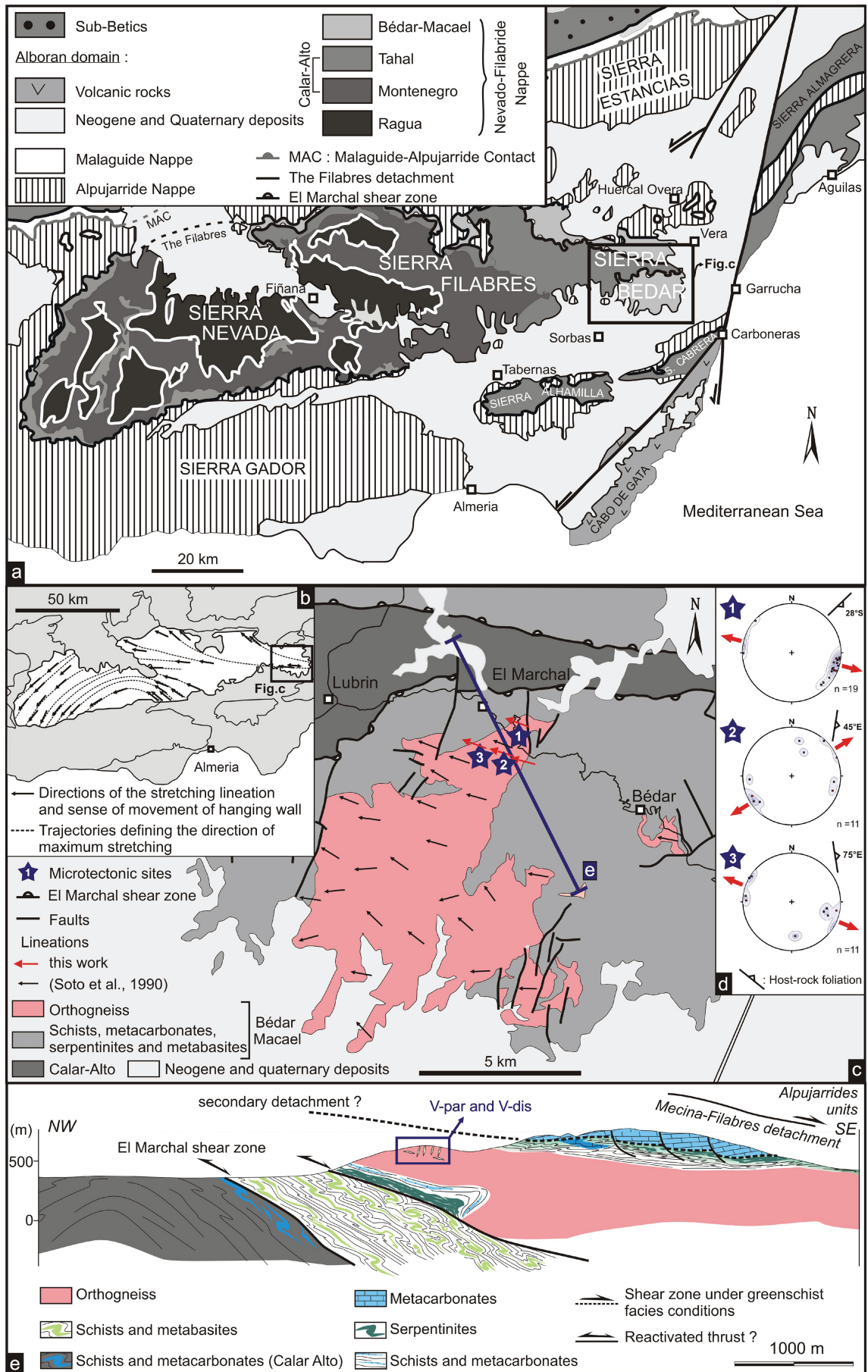


Figure 1

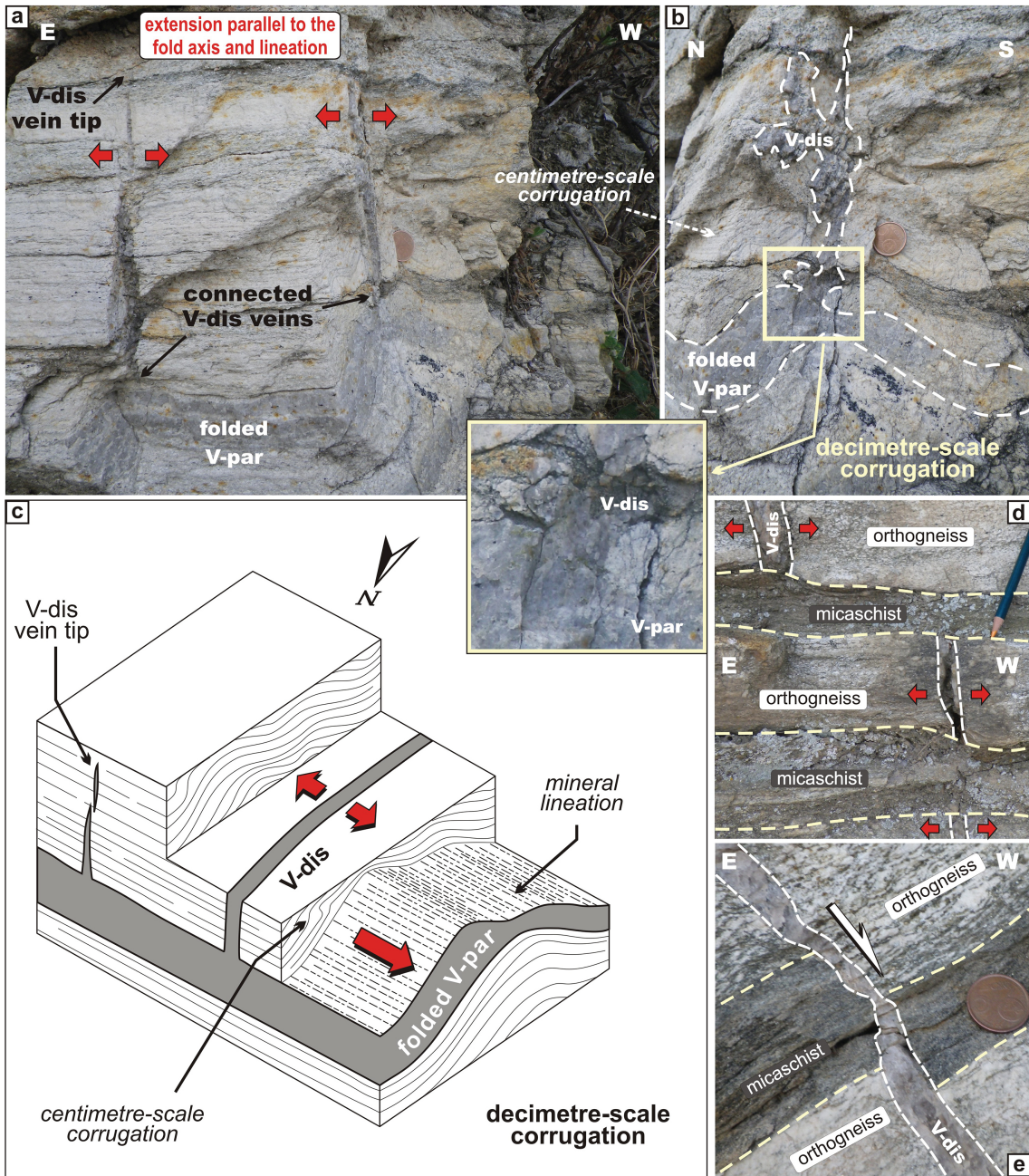


Figure 2

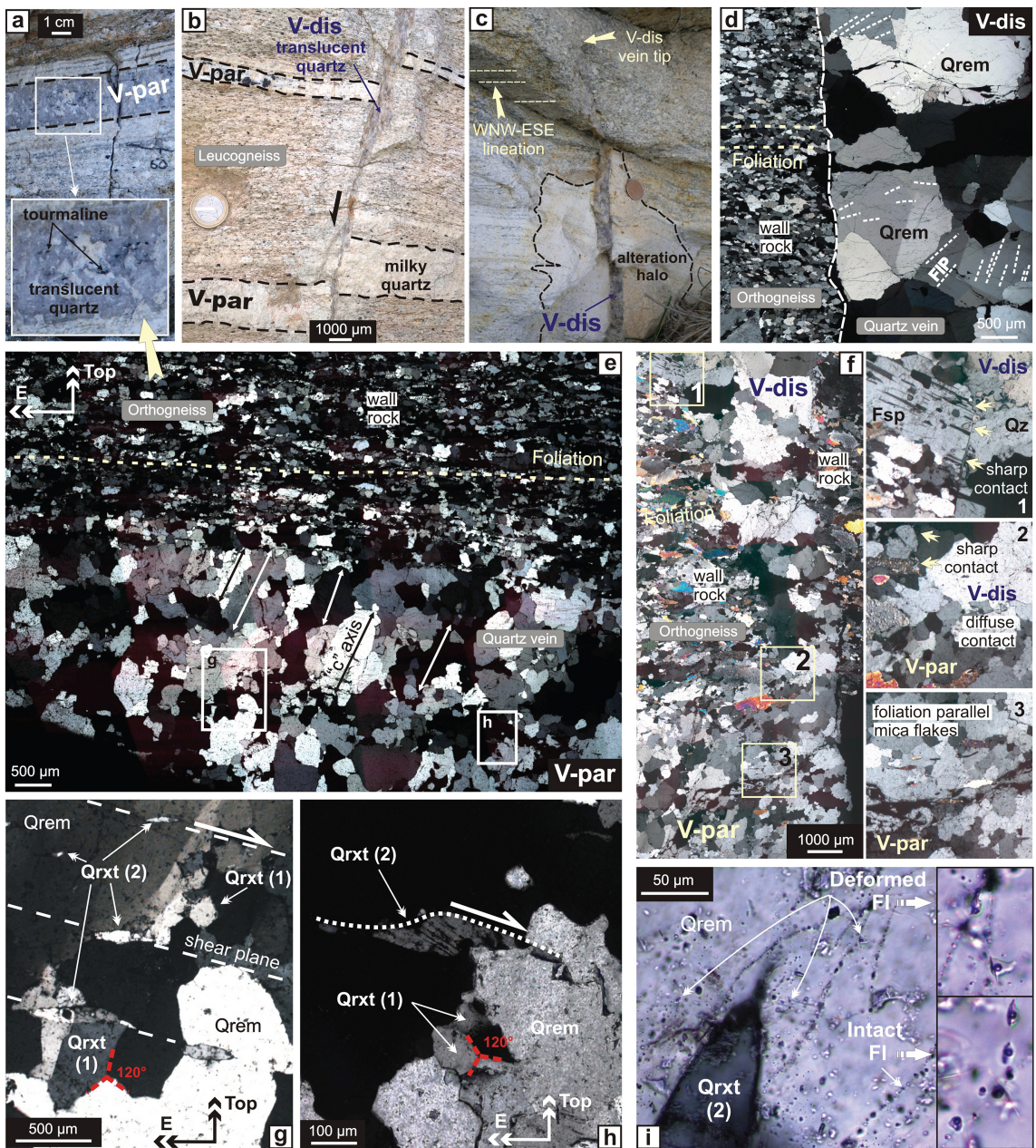


Figure 3

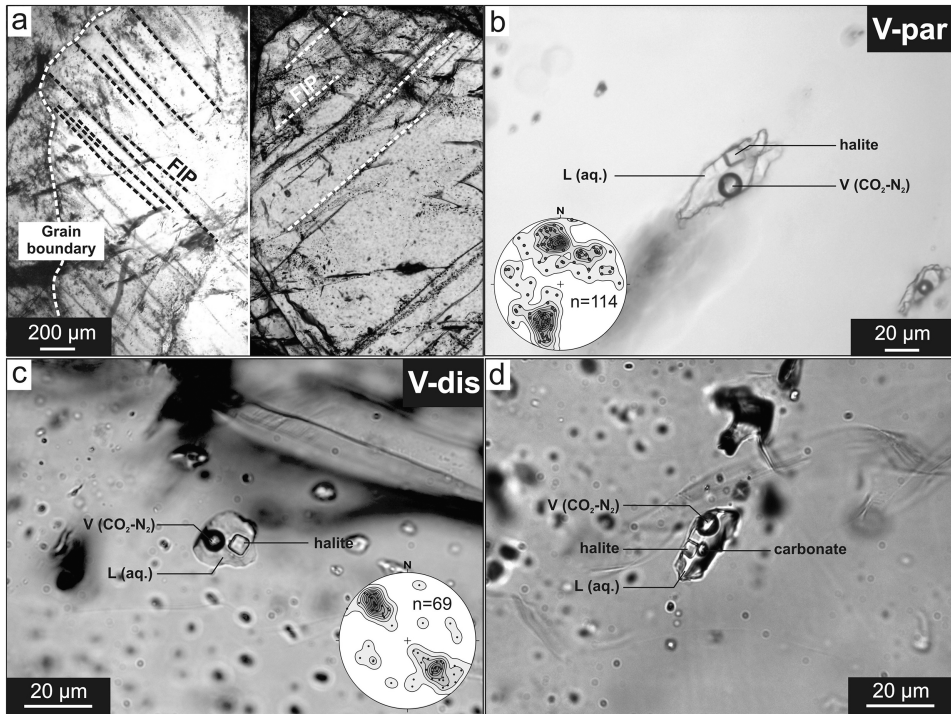


Figure 4

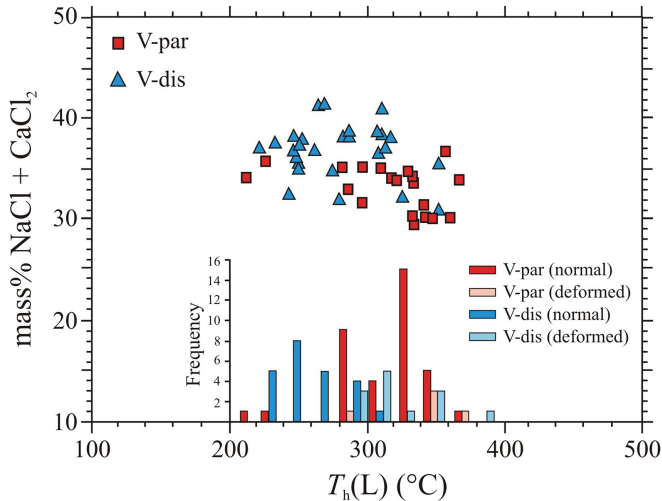


Figure 5

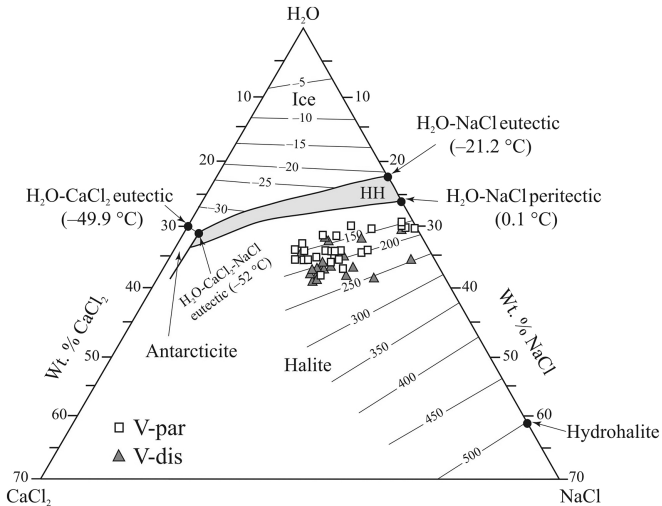


Figure 6

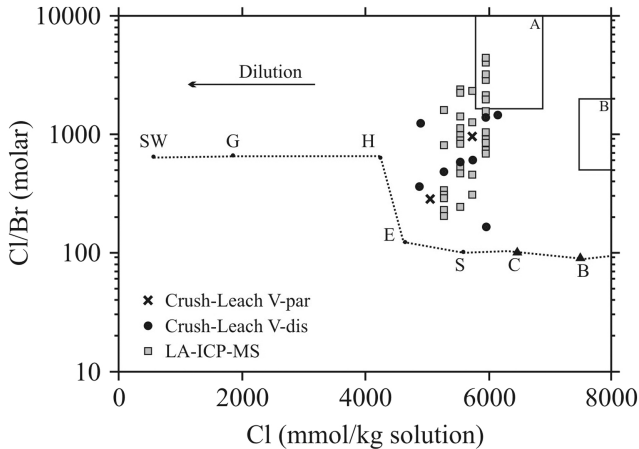


Figure 7

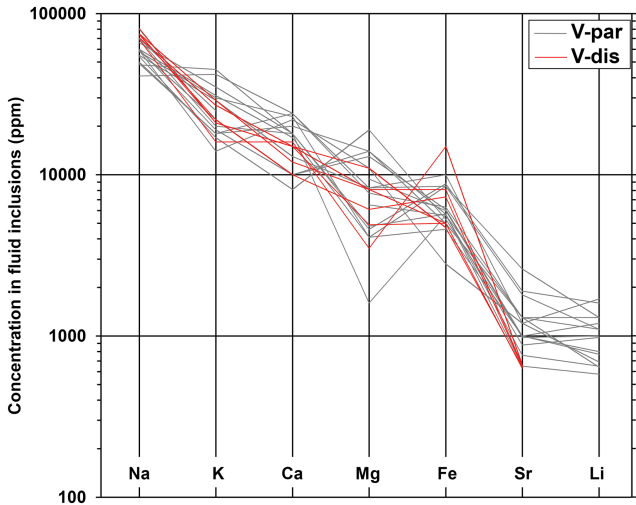


Figure 8

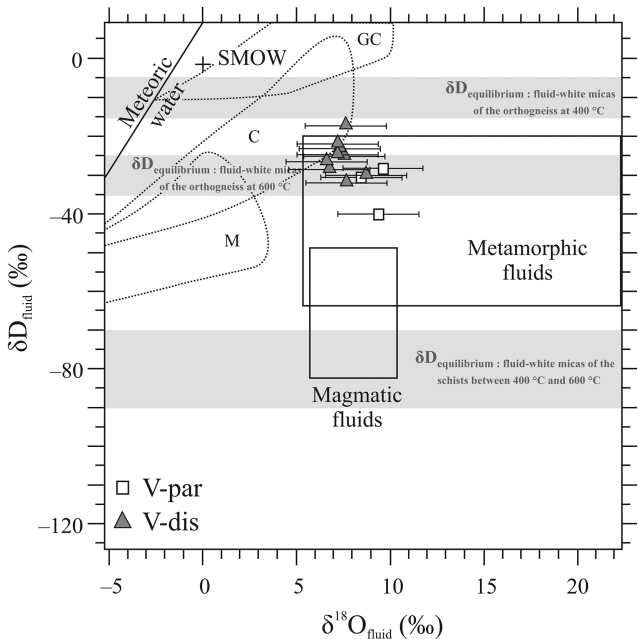
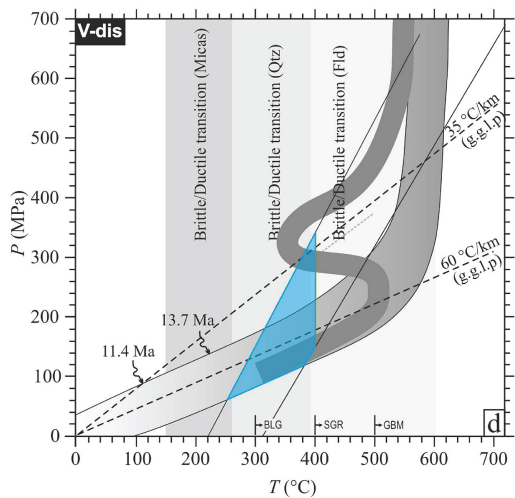
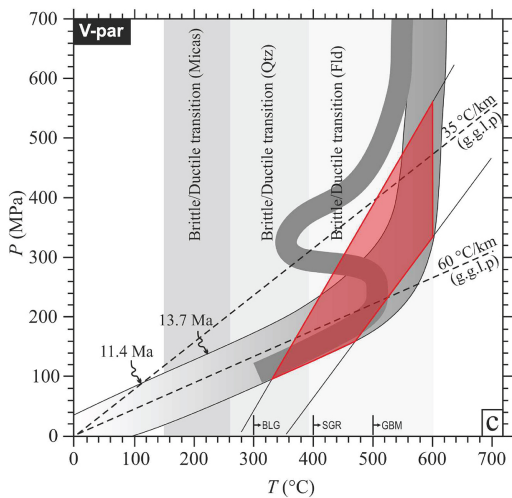
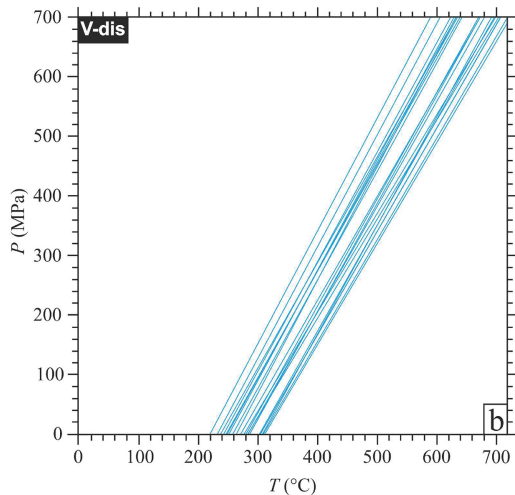
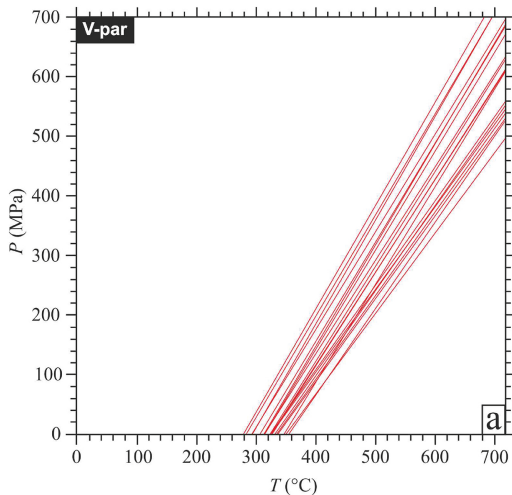


Figure 9



- Isochores of fluids in V-par
- Isochores of fluids in V-dis
- Range of P - T trapping conditions for fluids in V-par
- Range of P - T trapping conditions for fluids in V-dis
- P - T path (De Jong, 1992)
- P - T path (Augier, 2005)

Figure 10

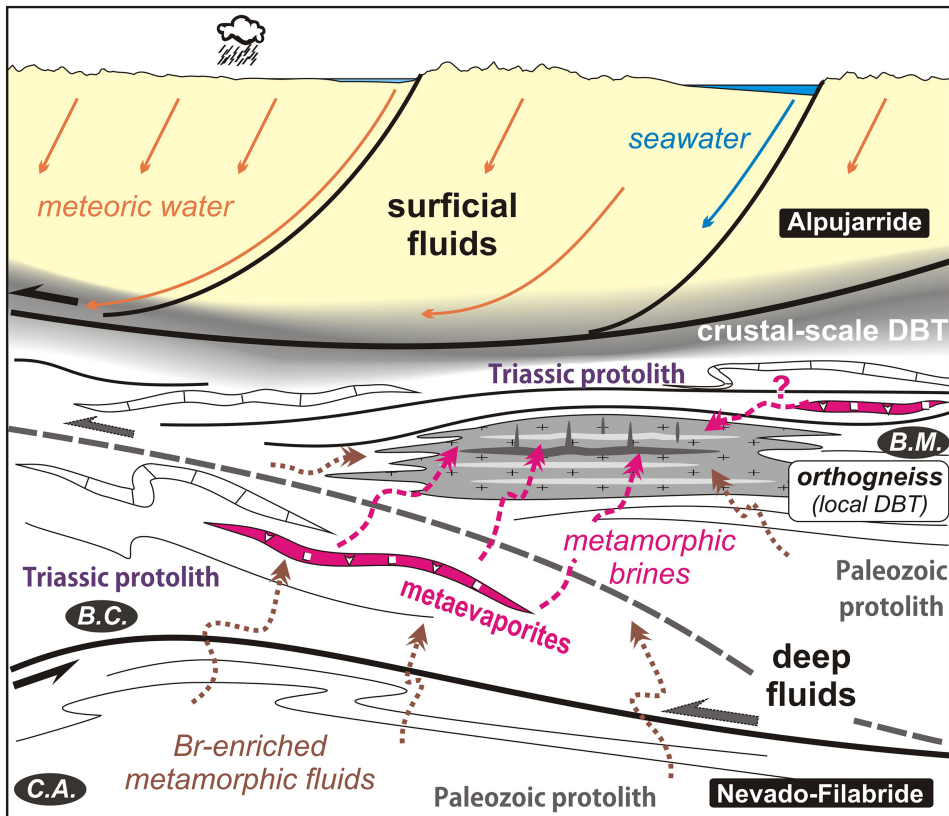


Figure 11

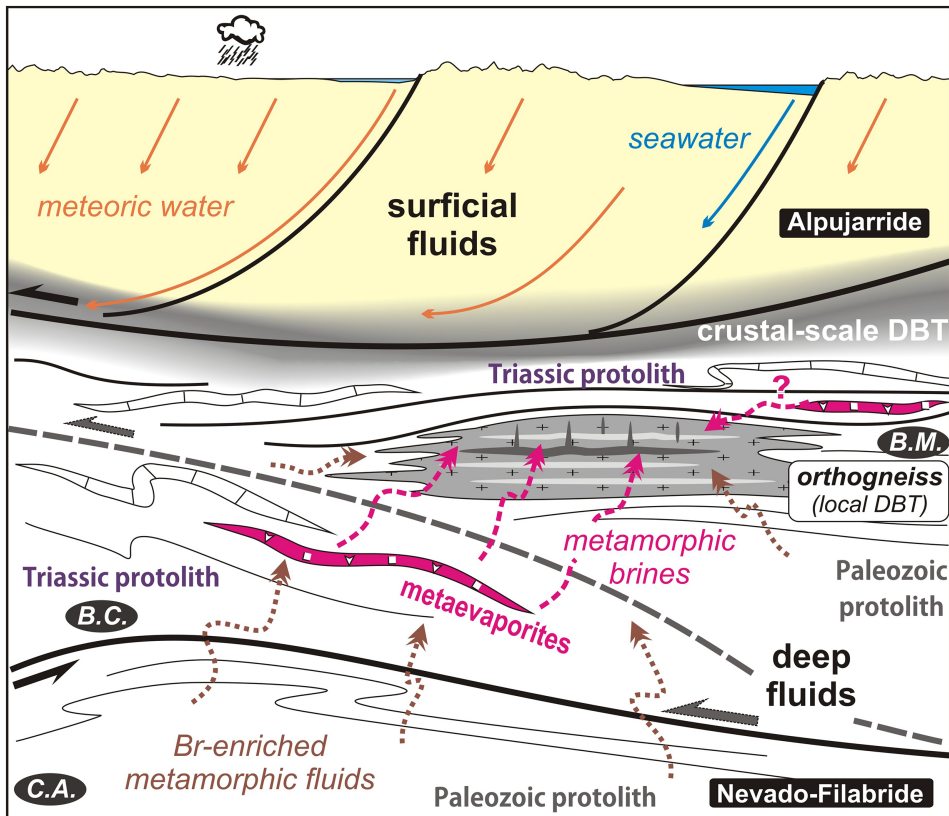


Figure 12